공학 박사 학위논문

Two-Dimensional Co-Compounded Nanoplates

2차원 혼성복합체 나노플레이트

2020년 2월

서울대학교 대학원

기계항공공학부

송 혜 린

Abstract

Two-Dimensional CO-Compounded Nanoplates

Hyelynn Song
School of Mechanical and Aerospace Engineering
Seoul National University

Various two-dimensional(2D) materials attract a lot of attention due to their structural characteristic and applicability. Crystalline 2D materials are being developed, and research on their application in various fields has been reported. Among those materials, graphene having a honeycomb lattice with six carbon atoms is one of the most popular materials due to its excellent physical and chemical properties. However, other carbonaceous materials are in the shadow of interest due to the prosperity of graphene's superior properties.

Due to the richness of information for organic chemistry, various forms of organic materials still have enormous opportunity to be developed. Based on the knowledge of organic chemistry, this thesis proposes a new concept of two-dimensional material. By combining the advantages of the materials involved in the reaction process, this new concept two-dimensional materials with the desired material properties can be synthesized. There may be two or more starting materials participating in the reaction.

In this thesis, two kinds of organic materials were used as starting materials to synthesize two-dimensional carbonaceous nanoplates with more sp^2 bonds than previously reported carbonaceous materials. The new class of carbonaceous compounds using organic (glucose) and other organic materials (1,2-dihydroxybenzene), which are organic-organic co-compounds are suggested here. We successfully synthesized two-dimensional carbonaceous material that can be synthesized in one-pot process without any by-products. The material characteristics of our synthesized co-compounded nanoplate (Co-CANP) were analyzed and its efficacy was confirmed by using it as a filler of various type of composite materials.

Keywords: co-compounded materials, co-compounding, two-dimensional material, nanoplate, carbonaceous material, hydrothermal carbonization, synthesis platform, viscosity-induced two-dimensional growth

Student number: 2014-30364

Contents

List of Tables

List of Figures

Chapter 1. Introduction

1.1 Carbonaceous materials

Carbon with atomic number 16 has been booming in various fields with the development of nanotechnology over the past three decades[1-9]. In particular, carbonaceous materials are in a spotlight as an alternative candidate of metal because of its light weight and excellent physical and chemical properties.

Allotropes of carbon are typically classified as graphite, diamond, carbon nanotube (CNT), fullerene and amorphous carbon [1, 10]. Many researchers have been interested in discovering pristine carbon materials, but they also have attempted to convert carbohydrates that are most abundant element in nature into carbonaceous materials.

Among variety of carbohydrates, monosaccharides which is the simplest form of sugar are most attractive renewable source because it can be expected that simpler form of carbohydrate is effectively converted into carbonaceous materials in a simpler way. There are various kinds of monosaccharides such as xylose, arabinose, glucose, fructose, d-galacturonic acid, ribose, deoxyribose and mannose [11]. These materials are qualified raw materials for synthesizing pristine carbonaceous materials as a precursor.

The hydrothermal synthesis is the typical thermochemical technique for converting carbohydrates into carbonaceous materials; it is called

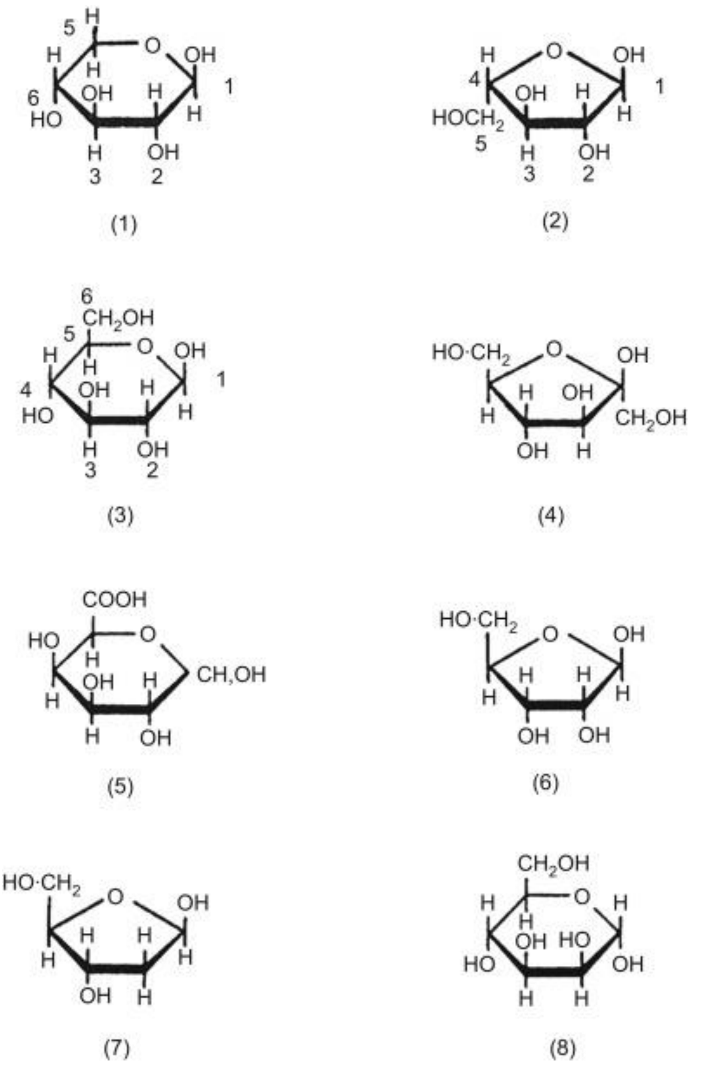

(1) (2)

(3) (4)

(5) (6)

(7) (8)

Figure 1-1. Structural representations of (1) xylose (β-d-xylopyranose), (2) arabinose (α-l-arabinofursnose), (3) glucose (β-d-glucopyranose), (4) fructose (β-d-fructofuranose), (5) d-galacturonic acid, (6) ribose (β-d-ribofuranose), (7) deoxyribose (β-d-deoxyribofuranose) and (8) mannose (α-d-manno-pyranose) [12]

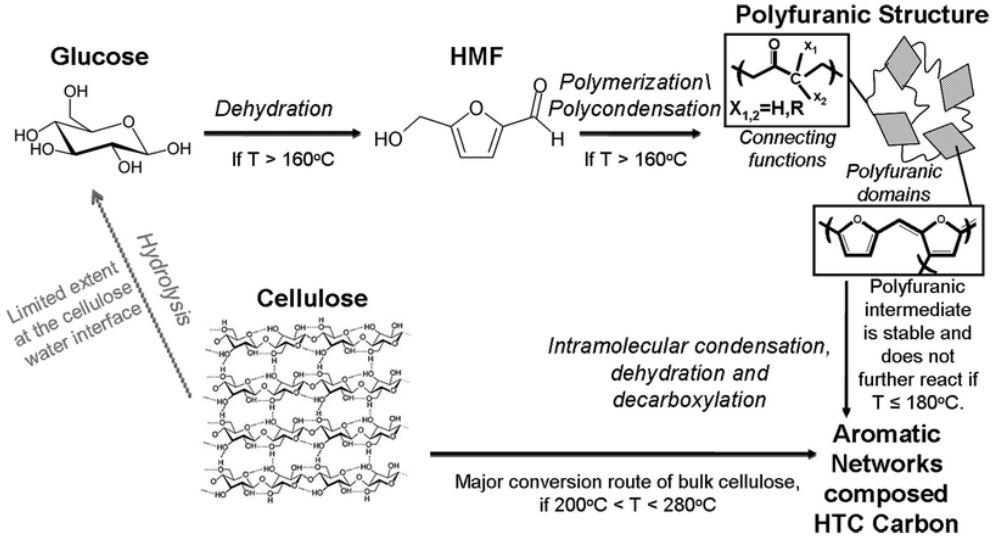

Figure 1-2. Hydrothermal carbonization model for glucose under mild processing conditions (180 °C < T < 280 °C) [13]

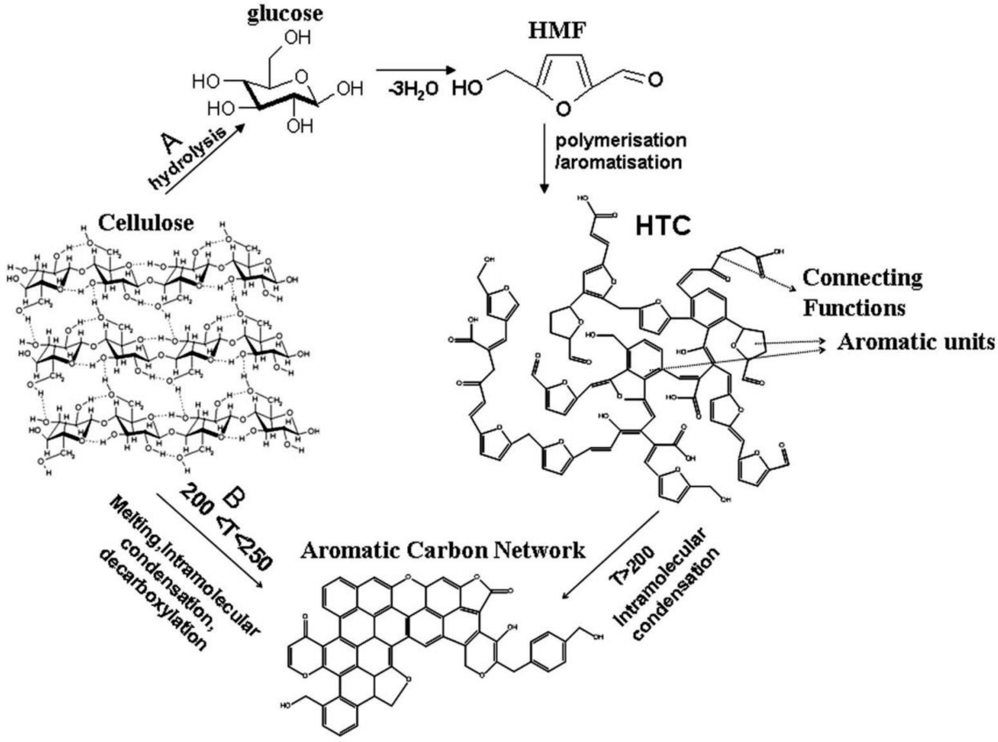

Figure 1-3. Conversion of cellulose into hydrothermal carbonization: (A) via HMF resulting in a furan-rich aromatic network and (B) direct aromatization [14]

hydrothermal carbonization (HTC). Hydrothermal synthesis is a method in aqueous media above boiling point of water in the high pressure autoclave which can prevent aqueous liquids decompose into gases. Hydrothermal carbonization using aqueous solution-filled autoclave have been generally used for converting monosaccharides into carbonaceous materials, its final products are zero-dimensional carbon spheres as shown in the Figure 1-4.

To synthesize other dimensional carbonaceous materials, various modified techniques were suggested [13, 15-20]. However, it is hard to synthesize pristine one-dimensional carbonaceous materials by chemical reaction of decomposed monosaccharides itself [15, 16]. On the other hand, two-dimensional carbonaceous materials can be synthesized by monosaccharides itself [21]. This two-dimensional carbonaceous material was synthesized on the basis of viscosity-induced two-dimensional growth of nuclei and is a two-dimensional version of carbon spheres. Two-dimensional nanoplates synthesized from carbohydrates can be evaluated as another two-dimensional carbon allotrope as graphene.

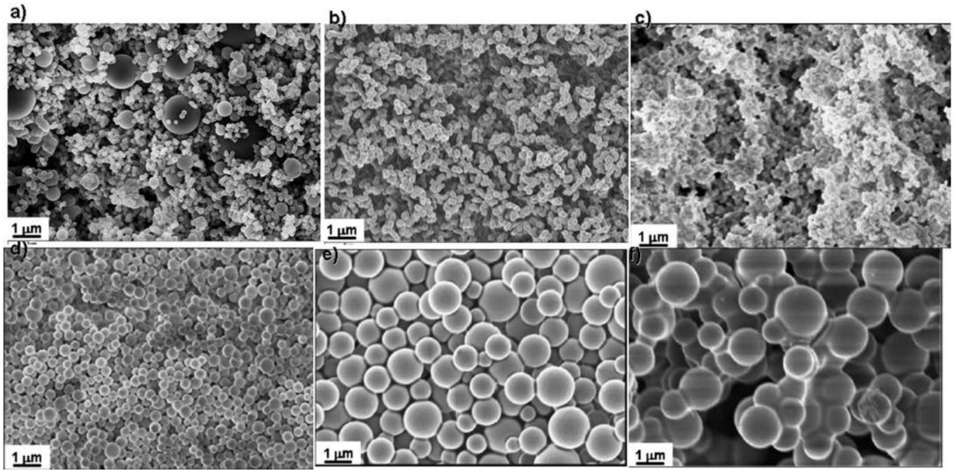

Figure 1-4. SEM micrographs of hydrothermal carbonization materials obtained at 180°C from: (a) glucose; (b) fructose; (c) hydroxymethyl furfural (HMF); (d) xylose; (e) furfural; and (f) sucrose [14]

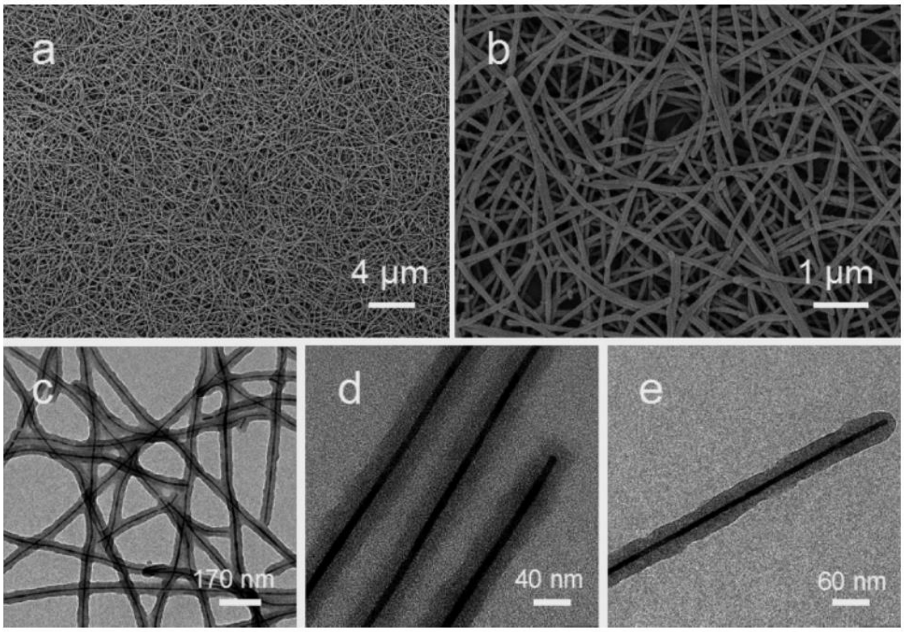

SEM and TEM images of the nanocables obtained from tellurium nanowires and glucose at 160 °C for 12 h [15]

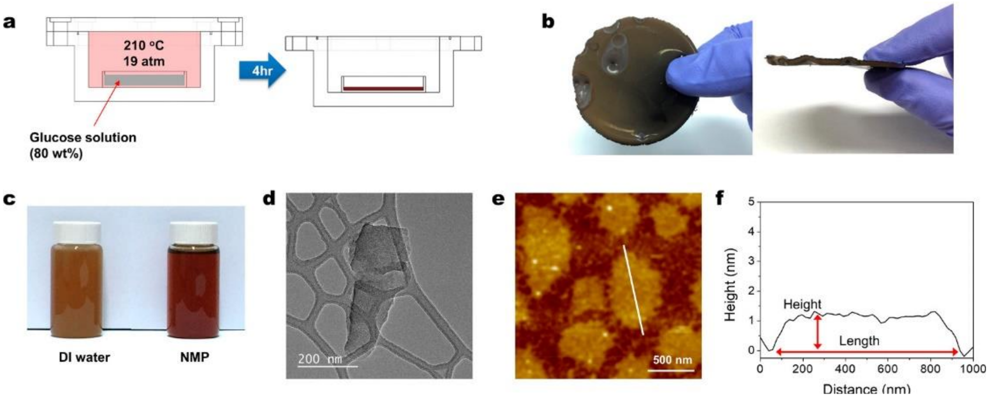

Figure 1-5. Synthesis method and characteristics of synthesized carbonaceous nanoplates (CANP). (a) Schematic of the device for synthesizing CANP. (b) Optical images of as-synthesized solid mat of CANP. (c) Colloidal solution of CANP dispersed in DI water and NMP (d) TEM image of CANP on carbon gird. (e) AFM image of CANP. (f) Height vs distance graph obtained along the white line in the AFM image of panel (e) [21]

1.2 Motivation and Research Objectives

Graphene has aroused popularity of two-dimensional materials due to its exceptionally outstanding properties. Despite the tremendous progresses made in the two-dimensional materials, carbonaceous 2D materials have not seen their light perhaps because of the overwhelming shadow cast by graphene and graphene oxide.

In this thesis, we introduce a platform for carbonaceous 2D materials that are co-compounded carbonaceous nanoplates (Co-CANP). An opening was established in the area recently in the form of carbonaceous nanoplates (CANP)[21]. This 2D material was synthesized on the basis of viscosity-induced two-dimensional growth of nuclei and is a two dimensional version of the well-known carbon spheres [13, 18, 20] typically synthesized hydrothermally from carbohydrates such as glucose in autoclaves. For the viscosity-induced 2D growth, vapor-filled autoclave instead of the usual liquid-filled one was used for the hydrothermal synthesis. Complete conversion of glucose to CANP made the synthesis separation-free. Green and clean synthesis involving only water and a renewable reagent is an attractive feature of CANP.

The ability to tailor a 2D material for better properties is quite desirable. One way of accomplishing the purpose is to synthesize a 2D material consisting of two compounds, i.e. co-compounded 2D material, each contributing its own character for better material properties. The advent of CANP suggests a two-dimensional material Co-CANP. In essence, Co-CANP to CANP is what copolymer is to polymer. Co-compounding carbonaceous nanoplates with another compound is accomplished by one-pot process and the synthesized Co-CANP does not require any separation for its use. The platform introduced here opens the door to organic-inorganic Co-CANPs and also to many component Co-CANPs.

To demonstrate the efficacy of Co-CANP, various applications were tested. Effects of Co-CANP are demonstrated in the tire rubber composite, sound absorption material, and thermal dissipation material.

Chapter 2. Co-Compounded nanoplates

To tailor a 2D material for better properties, bottom-up synthesis is the proper approach. One way of accomplishing the purpose is to synthesize a 2D material consisting of two kinds of compounds, i.e. co-compounded 2D material, each contributing its own character for better material properties. Co-Compounded nanoplate (Co-CANP) was synthesized by viscosity-induced 2D growth, vapor-filled autoclave instead of the usual liquid-filled one was used for the hydrothermal synthesis.

Chapter 2 describes the synthesis of Co-CANPs and optimizing conditions for high aspect ratio with atomic thickness. In addition, the characteristics of the synthesized Co-CANP measured using a variety of equipment to examine the material properties of Co-CANP.

2.1 Synthesis of two-dimensional co-compounded nanoplates

2.1.1 Source materials

To synthesize carbonaceous material by thermochemical reaction, monosaccharides having the simplest structure among the sugars was used as a nuclei source to facilitate the reaction. Glucose was chosen because it is most abundant form of monosaccharides. Furthermore, glucose has proven as an effective nuclei source for synthesizing carbonaceous materials [13, 20, 21]. 1,2-dihydroxy benzene (DHB) was used as a building block material, which has a hydroxyl group that reacts with the oxygen functional groups of glucose to form a continuous carbon network. In addition, DHB has aromatic ring composed of sp^2 hybridization. The structural properties of DHB are expected to play a large role in increasing the amount of graphitic structure with hexagonal ring structure in the synthesis of Co-CANP. Figure 2-1 shows that solution of glucose and DHB mixture in DI water is well dispersed at concentration of 80 wt% when the solution is heated at 90°C of water bath.

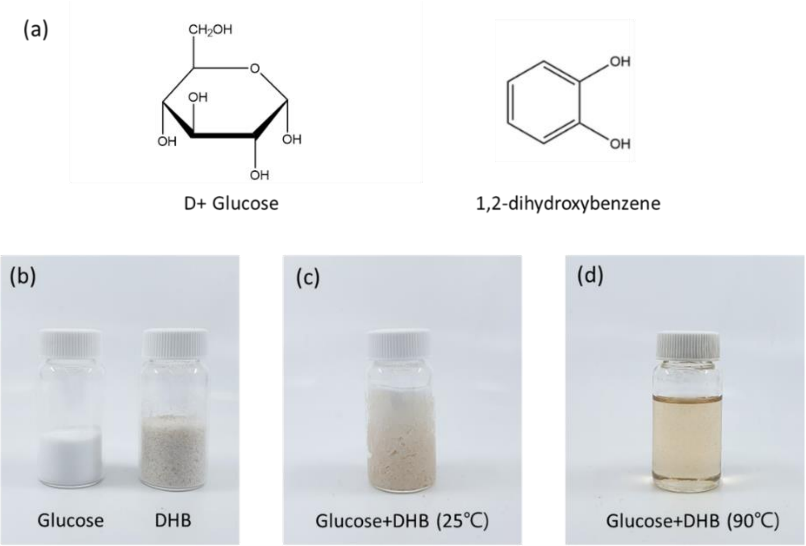

Figure 2-1. (a) Chemical structure of D+ Glucose (denoted as glucose) and 1,2-dihydroxybenzene (denoted as DHB) (b) optical image of raw material state for glucose and DHB (c) undissolved 80 wt% solution of glucose and DHB mixture at room temperature (d) completely dissolved 80 wt% solution of glucose and DHB mixture in water bath at 90°C.

2.1.2 Vapor-filled hydrothermal synthesis

Vapor-filled hydrothermal method is a modified hydrothermal process using superheated vapor. All liquid phase water inside autoclave evaporated at much higher temperature than boiling point of water, thus it turned into superheated vapor. All water molecules were vaporized in the closed system so that there is no water within glucose and DHB mixture. High concentration mixture composed of two kinds organic sources grew along the lateral (in-plane) direction without any disturbance from water molecules as shown in Figure 2-2. The bonds between two precursor materials are formed only in the in-plane direction, so that the two-dimensional material is finally synthesized. Therefore, suggested vapor-filled hydrothermal method is much more beneficial for synthesizing 2D materials with high aspect ratio due to anisotropic nature of induced pressure. The higher the viscosity of solution, the more capable of synthesizing a 2D material with a higher aspect ratio as previously reported CANP [21]. The difference from the conventional liquid-filled hydrothermal method is as follows; vapor-filled hydrothermal synthesis uses an exact amount of water to meet the required saturated steam pressure by considering the volume of the autoclave. Therefore, in the temperature above the boiling point of water, the vapor-filled hydrothermal synthesis method is present in all water forms as a gas, but the liquid-filled hydrothermal synthesis method is present as two phase of water; gas and liquid that cannot be gasified due to saturated steam.

For this reason, the vapor-filled hydrothermal method does not receive any force in the in-plane direction because the water in the mixture solution of glucose and DHB does not remain in the liquid state but all exist as vapor state at elevated temperature during the hydrothermal carbonization reaction.

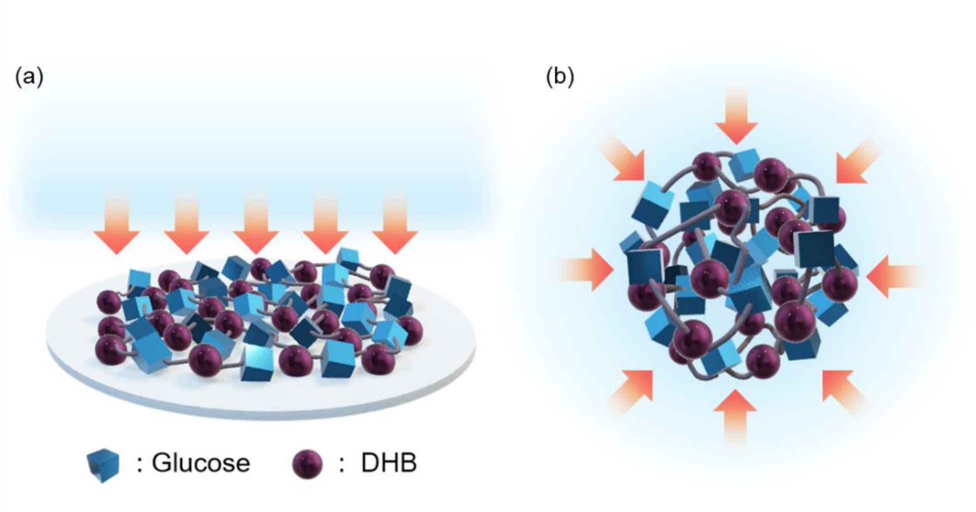

Figure 2-2. Schematic illustration of (a) vapor-filled hydrothermal synthesis, and (b) conventional liquid-filled hydrothermal synthesis

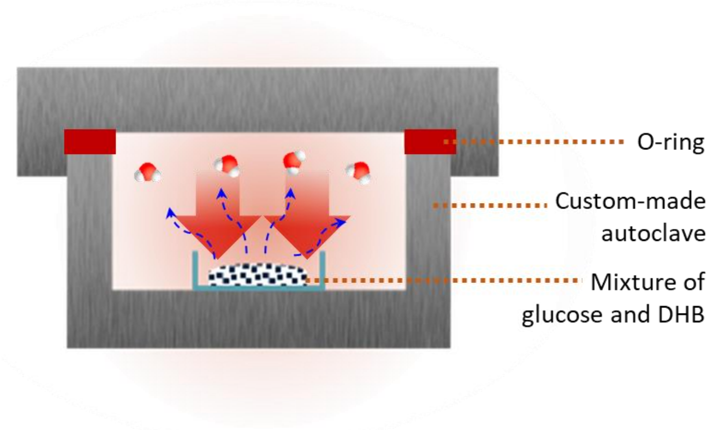

Figure 2-3. Schematic illustration of autoclave settings

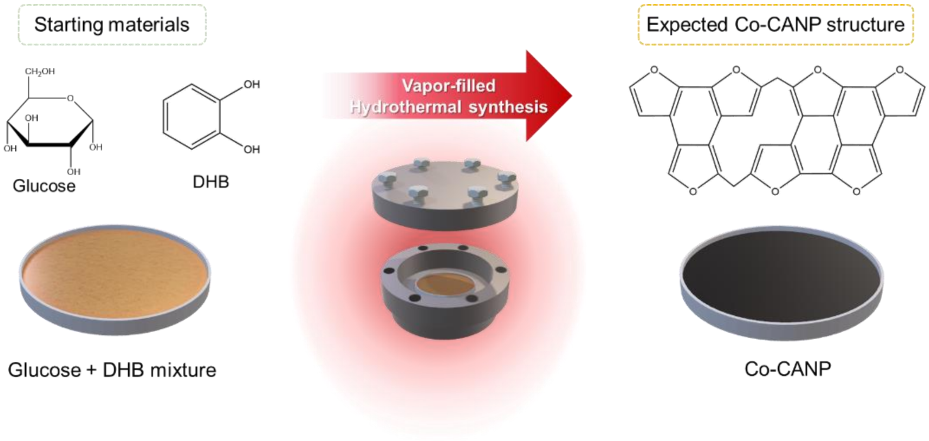

Figure 2-4. Schematic diagram of overall process for synthesizing Co-CANP using glucose and DHB by vapor-filled hydrothermal synthesis method

Figure 2-5 show the front and side views of the damp solid mat of Co-CANP taken out of the autoclave at the end of the synthesis. No reactants remained in the petri dish after the completion of the synthesis, indicating complete conversion of the reagents. The conversion yield of Co-CANP is 76% compared to source materials.

The synthesized Co-CANP can be made into fine powder using a pestle. Dissolving the synthesized Co-CANP powder in DI water at a concentration of 5 mg/ml, and then sonication was performed. It is well dispersed in water, but after 24 hours it can be seen that most of all subsided as shown in figure 2-6. To inspect dispersion characteristics precisely, it was evaluated by dissolving 1mg/ml of Co-CONP under optimal conditions in 20 kinds of organic solvents. In Figure 2-7, the organic solvent is the more polar solvent toward the right side. The higher the polarity of the solvent, the better the dispersion of Co-CANP. Among them, the dispersion of Co-CANP is excellent in DMF, DMSO, and NMP.

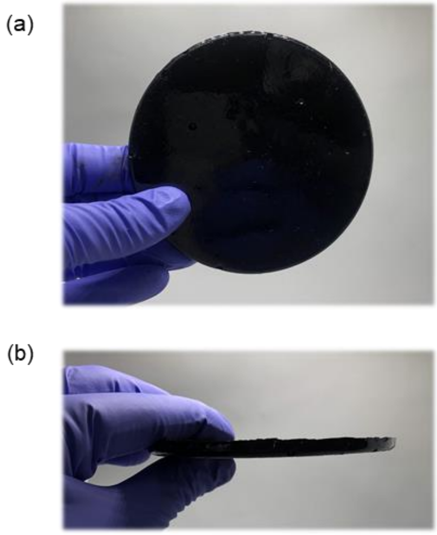

Figure 2-5. (a) Front and (b) side views of the damp solid mat of Co-CANP taken out of the autoclave at the end of the synthesis

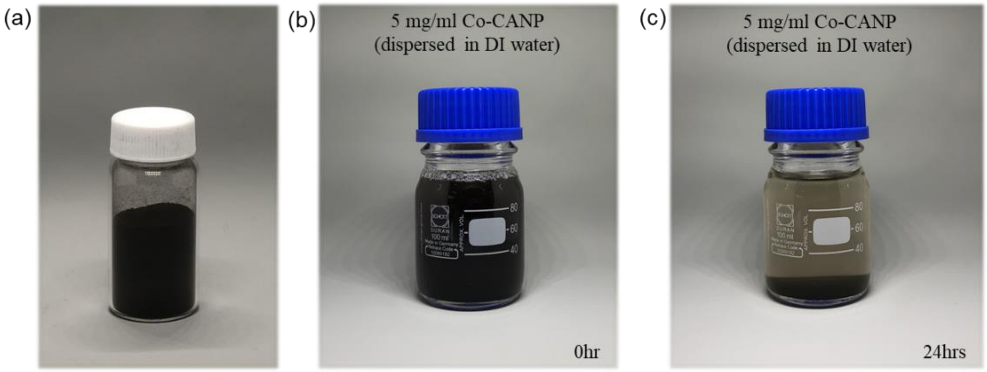

Figure 2-6. optical image of (a) Co-CANP in ground powder form (b) ultrasonication treated Co-CANP solution dispersed in DI water with concentration of 5 mg/ml (c) after 24 hours of ultrasonicated Co-CANP solution

Figure 2-7. Dissolving 1mg/ml of Co-CANP in 20 kinds of organic solvents (more polar to the right side)

Two dimensional nanomaterials are typified by nanometer scale thickness and relatively large length, or a high aspect ratio. To synthesize Co-CANP with a high aspect ratio, the mixing ratio of DHB to glucose was varied under otherwise the same conditions. The amount of DHB relative to glucose was increased from 10% to 60 wt% in increments of 10 wt%. Figure 2-8 shows the geometric features of the Co-CANP as affected by the mixing ratio. The actual topographical images of AFM are given in Figure 2-8 and the measurement results of approximately 200 nanoplates for each case by AFM for the averages of the thickness, the length, and the aspect ratio are shown in Figures 2-9(a) through (c). In general, the aspect ratio increases with increasing DHB ratio, showing a peak at 50 wt% of DHB and then falling to a small number at 60 wt%. The height, however, is larger for larger ratio, reaching up to 2.5 nm. The reaction at 60 wt% was incomplete as evidenced by the product mixture remaining in liquid state at the end of the reaction. An examination of the sample with Fourier transformation infra-red (FTIR) spectroscopy revealed the presence of DHB in the product mixture. All the results presented, unless otherwise noted, are for the DHB mixing ratio of 50 wt% that yielded the highest aspect ratio.

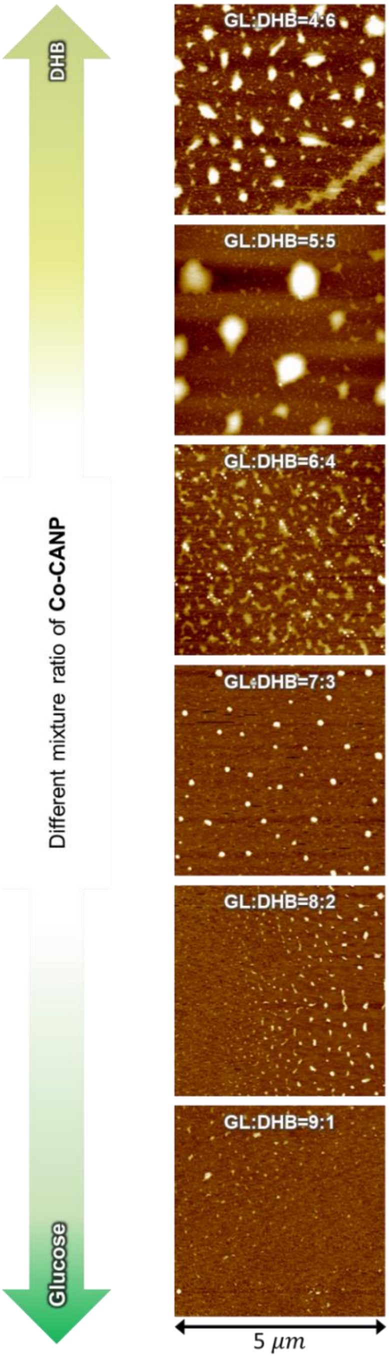

Figure 2-8. 5 μm scan-size images of AFM for Co-CANP for various mixing ratios of glucose to DHB

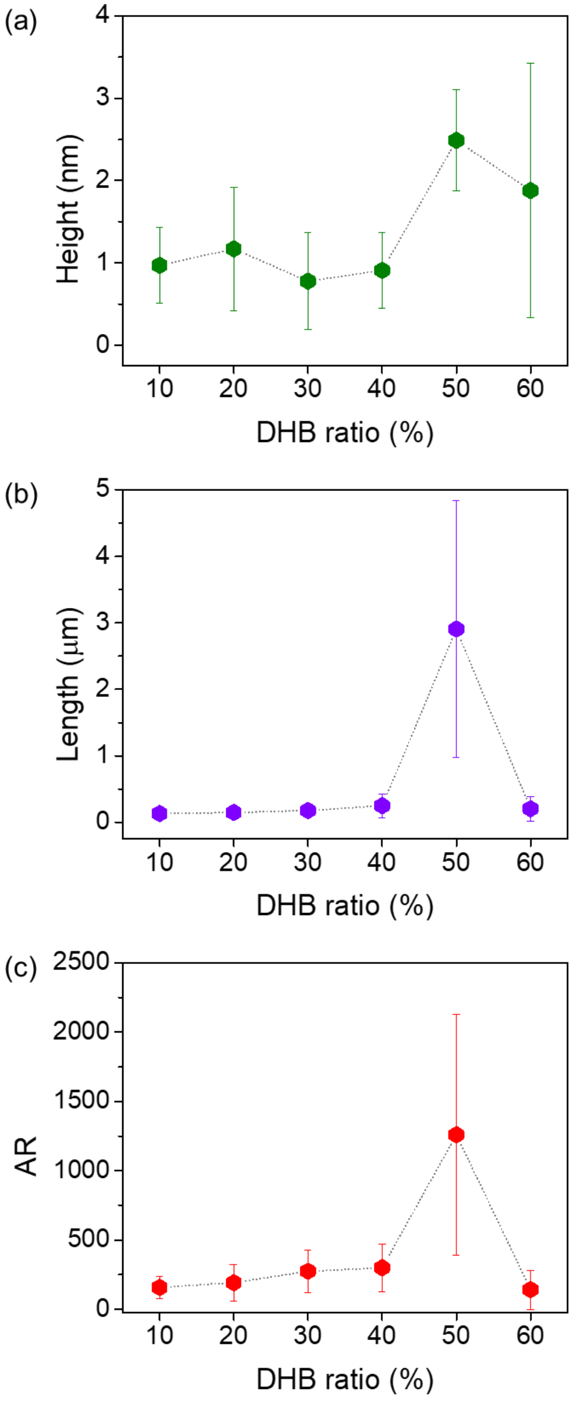

Figure 2-9. Changes in (a) height, (b) length, and (c) aspect ratio of Co-CANP as affected by the DHB mixing ratio

2.1.3 Mechanism of hydrothermal carbonization

As previously reported studies about hydrothermal carbonization of carbon spheres, its growth mechanism conforms to La Mer model [22, 23] as shown in Figure 2-10. As the hydrothermal process proceeds, the concentration of mixture solution increases and then formed high viscous solution. The intermolecular dehydration reactions are occurred between the hydroxyl groups attached to the glucose and DHB, and then it leads to polymerization. This indicates that some aromatic compounds and oligosaccharides are formed. The burst of nucleation occurs in the critically supersaturated state. And then, carbonization step proceeds [19].

The resulting nuclei grow by the diffusion of surrounding solutes. At this moment, the dimension of growing carbonaceous materials is determined by the direction of growth. If the solute is surrounded by a solvent, diffusion of the solute occurs isotropically, and grows into a sphere. This is the carbon spheres synthesized by conventional liquid-filled hydrothermal synthesis. On the other hand, two-dimensional carbonaceous nanoplates are synthesized inside an autoclave with no liquid phase water, so that anisotropically diffused solutes grow in a planar direction under high pressure.

To explain the chemical structure in detail, it is essential to account for the structural changes in the two organics that occur during decomposition and dehydration. As shown in Figure 2-11, Glucose is converted to 5-(hydroxylmethyl) furfural (HMF) by decomposition and dehydration [24], forming a network of furan and arene rings [25]. On the other hand, DHB forms a network composed of arene rings only due to its original chemical structure. Thus, when glucose and DHB react simultaneously, a network in which furan and arene coexist. This can be expected to improve the physical properties such as electrical and thermal conductivities [26, 27] because there are more arene ring consisting of sp^2 bonding than carbonaceous material derived from glucose only.

Figure 2-12 is a schematic diagram of the growth model of Co-CANP. First, glucose converted to fructose through isomerization. And then, dehydration occurs between the oxygen functional groups of fructose, thus it leads to converting fructose to HMF. Through hydrothermal carbonization, HMF undergoes polymerization and aromatization to form a carbonaceous complex consisting of aromatic rings and connecting functions. Thereafter, the intermediate produced by HMF has a hydroxyl group and a carbonyl group, and reacts with a hydroxyl group of DHB to undergo dehydration. The dehydration leads to build up bridge between the two oxygen functional groups, thereby expanding the network. Finally, intermolecular condensation occurs over a temperature range of 200°C or more, the final result of aromatic network is formed [14].

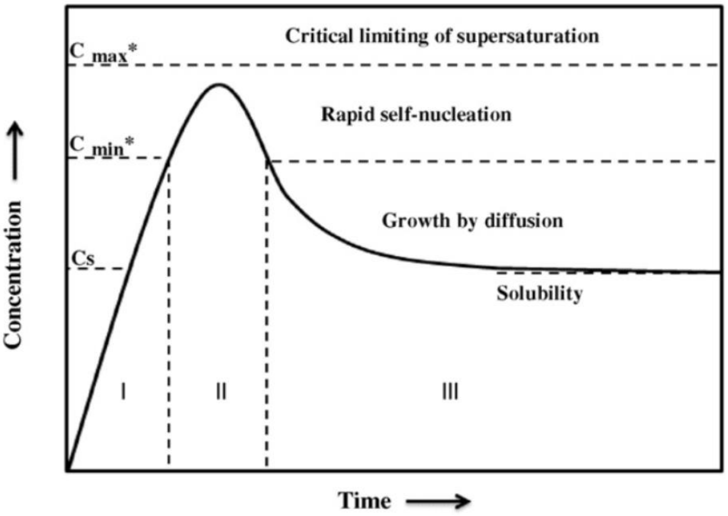

Figure 2-10. La Mer model. Early stage of the nucleation (I), nucleation period (II), crystal growth period (III). C_s: solubility; C_{min}^*: minimum concentration of nucleation; C_{max}^*: maximum concentration of nucleation [22, 23]

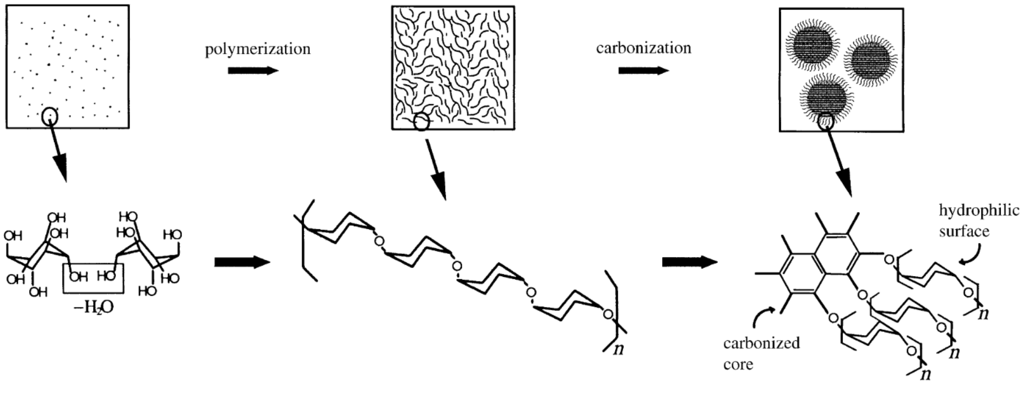

Figure 2-11. Schematic growth model for hydrothermal carbonized carbon sphere by dehydration [19]

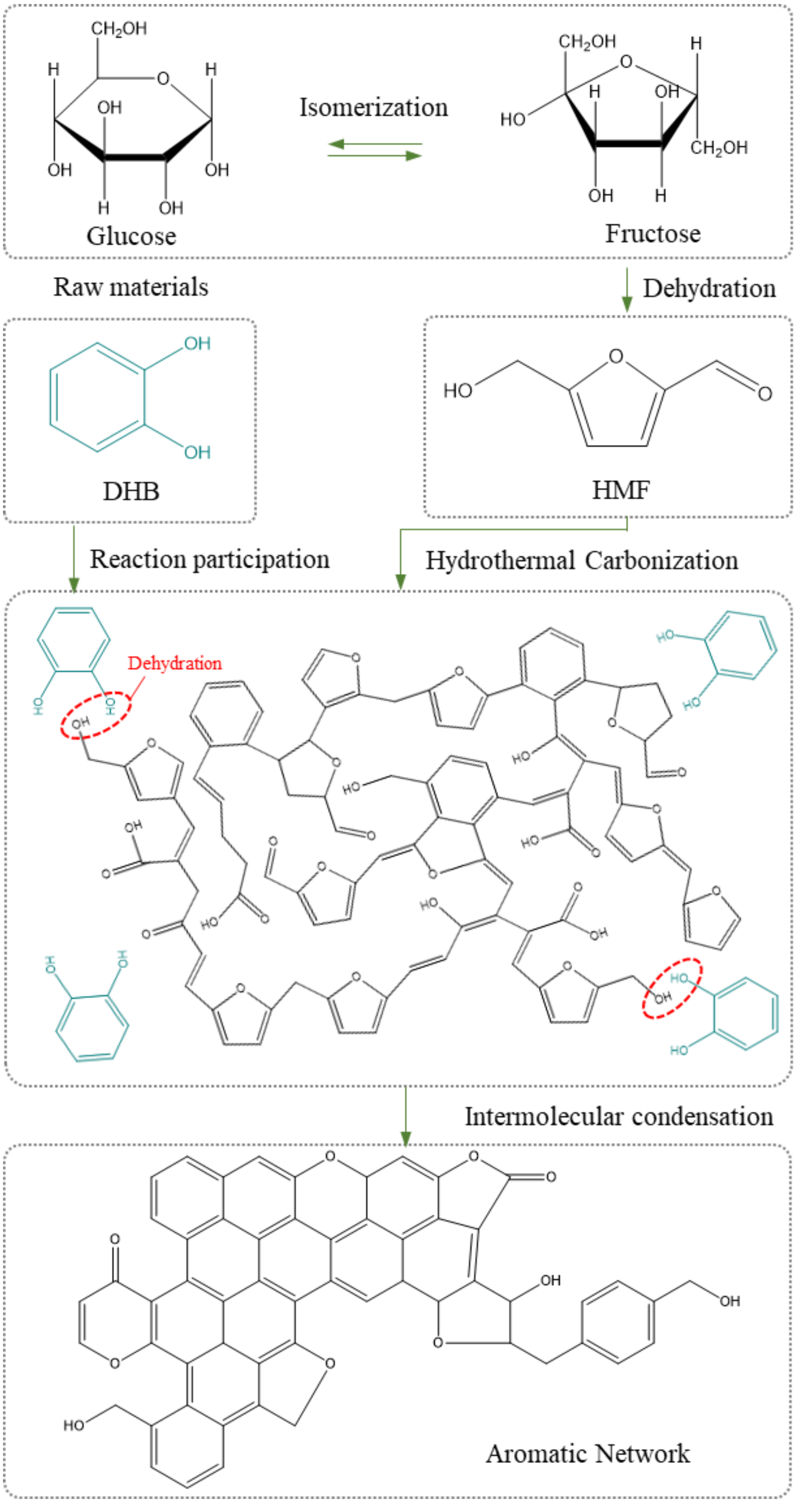

Figure 2-12. Schematic growth model for Co-CANP

2.2 Characterization of Co-Compounded nanoplates

This chapter demonstrates the successful synthesis of two-dimensional carbonaceous nanoplates through diverse analytical techniques. Various types of microscopes were used to observe the morphological characteristics of the synthesized Co-CANP, and the chemical nature of Co-CANP was investigated using spectroscopic techniques.

2.2.1 Microscopy

2.2.1.1 Scanning electron microscope (SEM)

Two-dimensional materials can be made into bucky papers by their morphological properties. Since Co-CANP also has a two-dimensional morphological characteristic, it was made into a bucky paper to observe the laminated structure of the Co-CANP by SEM. The bucky paper made by vacuum filtration of Co-CANP dispersed in DMF is shown in Figure xx. The top and side view of the bucky paper were observed. As shown in Figure 2-13, top view shows the structure is uniformly stacked along the plane direction. The side view shows the well stacked nanoplates layer by layer.

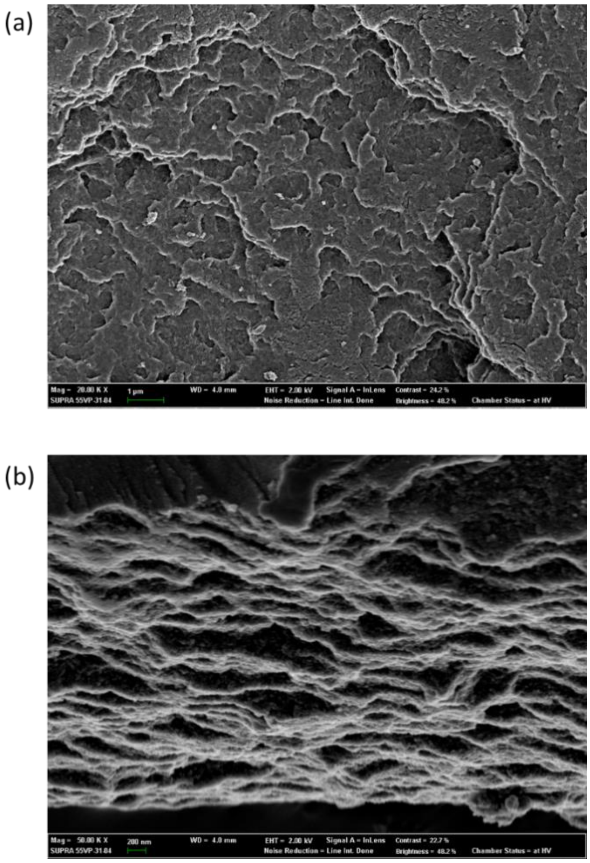

Figure 2-13. SEM images of the bucky paper obtained by vacuum filtration of Co-CANP dispersed in DMF: (a) top view (b) side view

2.2.1.2 Transmission electron microscope (TEM)

High resolution transmission electron microscope (JEOL, JEM-3010) were used to inspect morphological characteristics of Co-CANP. In order to prepare a sample for measurement, Co-CANP dispersed in DMF was coated on holey carbon film (200 mesh) by drop casting, and then completely dried under vacuum condition at 80°C.

In Figure 2-14, TEM images reveal the plate structure of Co-CANP. It is thin enough that the carbon grid below the Co-CANP can be identified. Several stacked nanoplates can be observed, which is indicated by dark shades. Due to the large aspect ratio, figure xx shows the wrinkled nanoplates. Size of nanoplates vary from hundreds of nanometers to several micrometers.

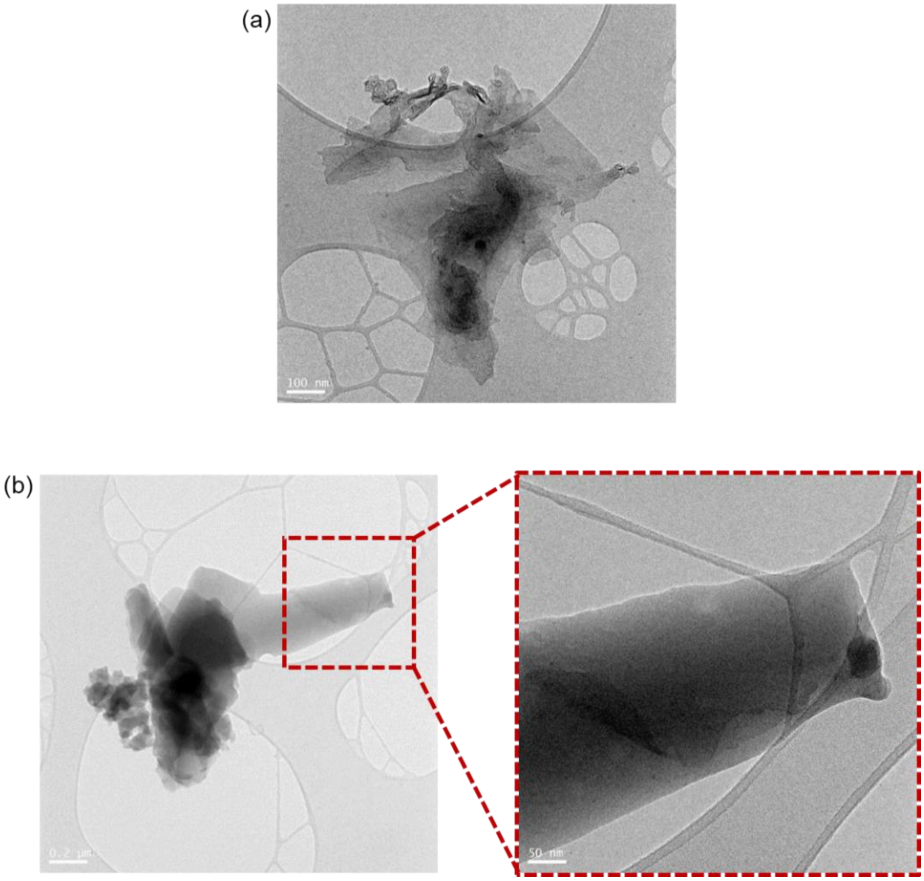

Figure 2-14. TEM images of synthesized Co-CANP (a) Co-CANP with a thickness thin enough to show a carbon grid (b) Co-CANP stacked in several layers

2.2.1.3 Atomic Force microscope (AFM)

To probe the physical nature of the 2D material in more detail, atomic force microscopy (AFM) was utilized. XE-150 (Park systems) was used under non-contact mode with 0.5 Hz of scanning rate. AFM images with scan size of 50 μm and 10 μm are shown in Figure 2-15 and 2-16(a).

The height and length profiles of two nanoplates in the AFM image in Figure 2-16(a) given in Figures 2-16(b) and (c). The results for the two nanoplates show that the thickness is less than 5 nm and the length is a few microns. The size distributions of the Co-CANP as determined by AFM with more than 200 nanoplates are given in Figures 2-17(a), (b), and (c), respectively, for the plate height, the length, and the aspect ratio, which is the ratio of length to height. The average height is 2.45 nm and the average length is 3.33 μm, yielding an average aspect ratio (AR) of 1620.

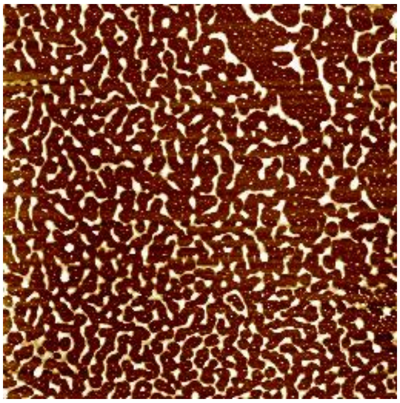

Figure 2-15. AFM image of Co-CANP (scan size: 50 μm)

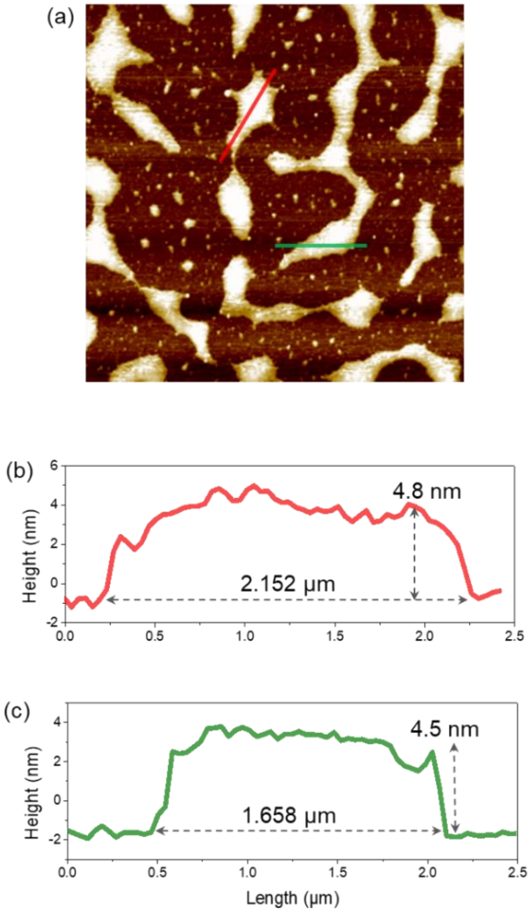

Figure 2-16. (a) AFM image of 10 µm scan size. (b-c) AFM morphological profiles of red and green line in AFM image of (a)

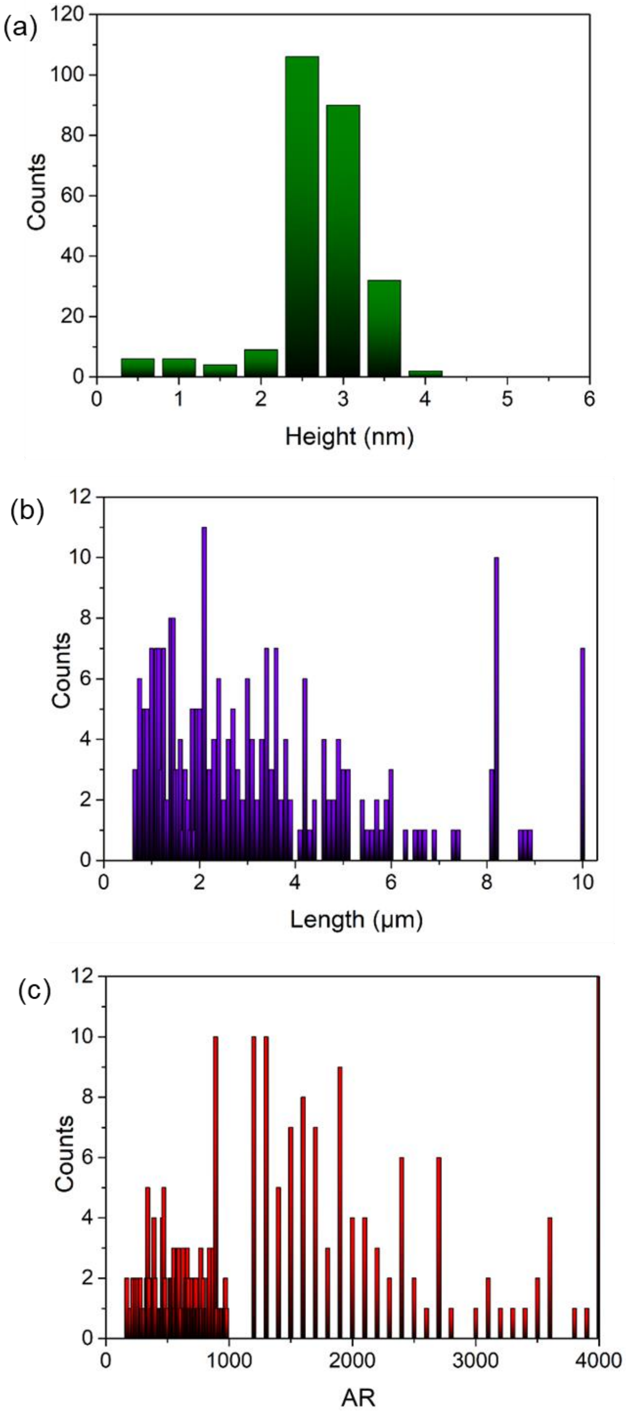

Figure 2-17. Size distributions of (a) height, (b) length, and (c) aspect ratio (AR)

2.2.2 Spectroscopy

2.2.2.1 nuclear magnetic resonance (NMR)

To gain a better understanding of the chemical structure of Co-CANP, ^{13}C solid-state nuclear magnetic resonance (NMR) spectroscopy was utilized. Figure 2-18 shows the spectra. The deconvolution results, obtained by Dmfit program [28], have peaks at 154 ppm (i region) and143 ppm (ii region) that represent C=C-O bond and C=CH-O bond of the furan ring, and peaks at 116 ppm and 110 ppm (vi region) that represent the C=C-O bond of the furan ring [29] . In addition, the sp2 bonding that represent arene ring appears at 130 ppm and 122 ppm (iii region). The two peaks at 73 ppm and 62 ppm (v region) indicate the hydroxyl group attached to this carbon skeleton [25, 30]. These results indicate that Co-CANP consists of interconnected furan and arene rings with oxygen functional groups.

It is of interest to find how the ratio of furan (denoted as “F”) to arene (denoted as “A”) in Co-CANP changes with the variation in the mixing ratio of DHB to glucose in the original reaction mixture. Figure 2-19 shows the NMR spectra of Co-CANP for various DHB mixing ratios, ranging from 10 wt% to 60 wt%. All the Co-CANPs synthesized, regardless of the DHB mixing ratio, have peaks in both regions of A and B in the NMR spectra. Region A in the figure consists of peaks representing furan and arene rings; region B consists of peaks representing aliphatic hydrocarbon. The figure indicates that the peak in the aliphatic region decreases with increasing DHB mixing ratio. When the mixing ratio is low as in the case of 10%, the two peaks in Region A for the furan and arene rings have a low intensity that is difficult to distinguish. As the DHB mixing ratio increases, the intensity of the peak is increased and sharpened. For the mixing ratio larger than 20 wt%, the two peaks are clearly visible.

To determine the furan-to-arene (F/A) ratio of Co-CANPs synthesized for different DHB mixing ratio, the method due to Falco et al. [29] was used as follows:

$$\mathrm{F/A} = \frac{4.5 \times \sum I\ (F, n)}{\sum I\ (A, n)}$$

where I(F, n) and I(A, n) are the integral values of the signals for furan and arene at certain ppm point (n), respectively. However, not all deconvolved signals are used for the F/A ratio. As previously reported, both signals at 122 ppm and 130 ppm representing arene are considered, but for furan only the signal represented by C= C-O at 110 ppm is considered. Table 1 shows integral values of deconvolved peaks for calculating furan to arene ratio (F/A). Based on this numerical values, F/A was calculated by equation 1. The results shown in Figure 2-20 reveal that the F/A ratio decreases with increasing DHB mixing ratio, indicating that more arene rings form as the DHB content in the reaction mixture increases, up to 50% DHB. When the DHB mixing ratio reaches 60%, however, the F/A ratio is shown to increase rather than decrease.

All the details of the deconvolved spectrum for each are shown in the Figure 2-21 to 2-26. As indicated earlier, the reaction does not go to completion when the mixing ratio is 60% and thus the data is not relevant for the full conversion being considered. Because of the highest arene content obtainable, the Co-CANP produced with the reaction mixture of 50% DHB is utilized in the applications involving Co-CANP. The analytical basis for this is discussed further in the FT-IR section.

The structural characteristics of Co-CANP and CANP (carbonaceous nanoplates synthesized using only glucose) also differ in the NMR spectrum as shown in Figure 2-27. Comparing the NMR spectra of CANP and Co-CANP, CANP shows a larger peak in the aliphatic region than Co-CANP. Also, the peaks of CANP exhibited by furan and arene at 100 to 170 ppm are weaker than that of Co-CANP's, which means that Co-CANP has more graphitic structure than CANP.

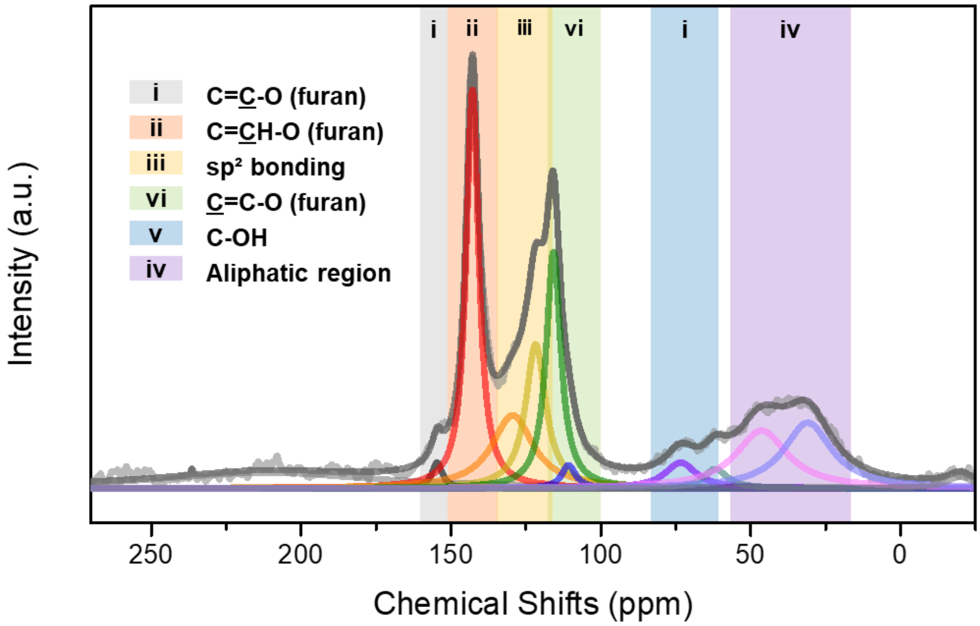

Figure 2-18. ^{13}C NMR spectrum of Co-CANP

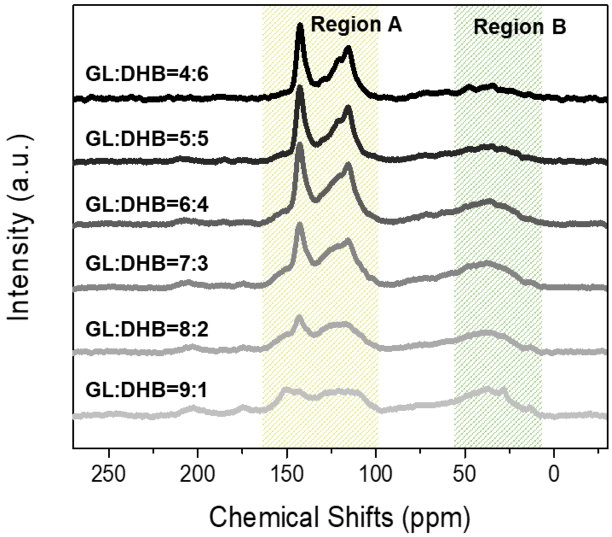

Figure 2-19. Comparison of NMR spectra according to glucose and DHB mixture ratio

	GL:DHB=4:6		GL:DHB=5:5		GL:DHB=6:4		GL:DHB=7:3		GL:DHB=8:2		GL:DHB=9:1	
	ppm	I	ppm	I	ppm	I	ppm	I	ppm	I	ppm	I
	153.72	0.37	154.85	0.67	153.90	3.50	153.57	5.47	151.94	5.86	150.63	18.13
	142.39	33.59	142.45	28.64	142.99	17.96	142.64	23.96	142.90	14.30	142.66	7.53
	129.89	**18.66**	**124.85**	**42.39**	140.01	9.03	**130.34**	**0.02**	**135.75**	**38.39**	**128.90**	**0.41**
	121.34	**18.77**	**121.30**	**7.44**	**122.30**	**54.98**	**123.43**	**56.22**	**125.41**	**19.23**	**122.28**	**66.54**
	115.37	26.63	115.44	20.47	115.22	13.87	115.09	12.38	115.90	19.53	113.59	3.69
	109.24	**1.99**	**110.50**	**0.39**	**109.71**	**0.67**	**108.40**	**1.95**	**108.49**	**2.70**	**108.70**	**3.70**
F/A	**0.239**		**0.035**		**0.055**		**0.156**		**0.211**		**0.249**	

Table 1. Integral values of deconvolved peaks for calculating furan to arene ratio (F/A). Peaks around 131 ppm and 125 ppm indicate arene, and peak around 110 ppm indicates furan (The values used for the F/A calculations are shaded by color)

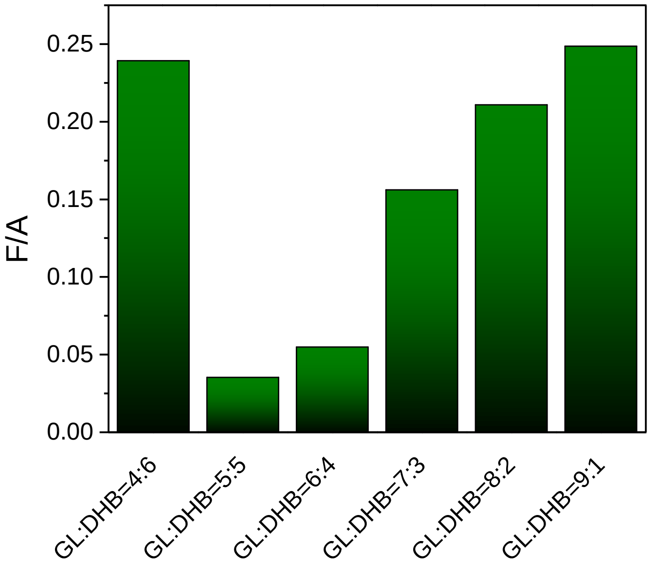

Figure 2-20. Calculated furan to arene ratio (F/A) according to glucose and DHB mixture ratio

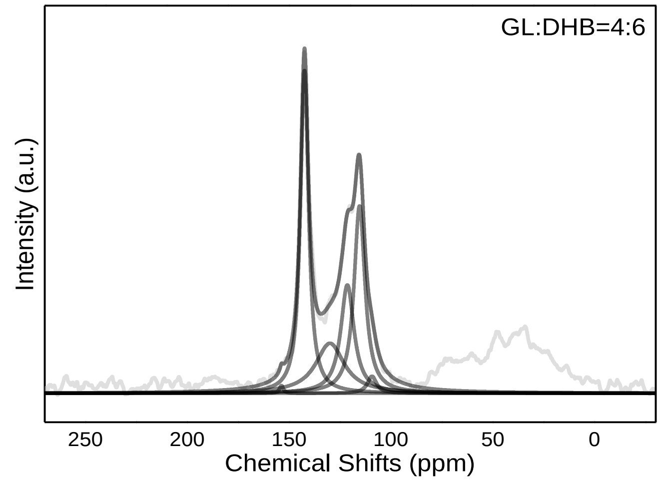

Figure 2-21. NMR spectrum of Co-CANP with Glucose to DHB ratio of 4:6 and its deconvolved peaks

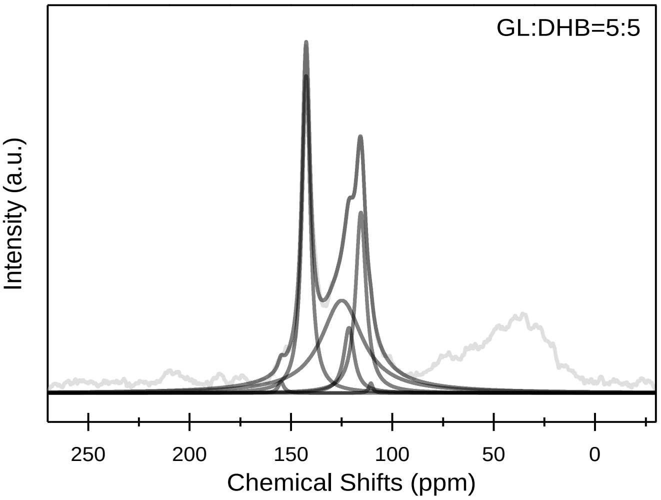

Figure 2-22. NMR spectrum of Co-CANP with Glucose to DHB ratio of 5:5 and its deconvolved peaks

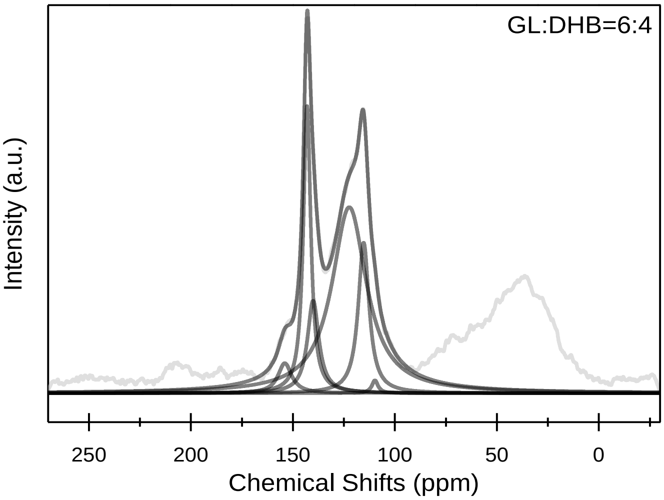

Figure 2-23. NMR spectrum of Co-CANP with Glucose to DHB ratio of 6:4 and its deconvolved peaks

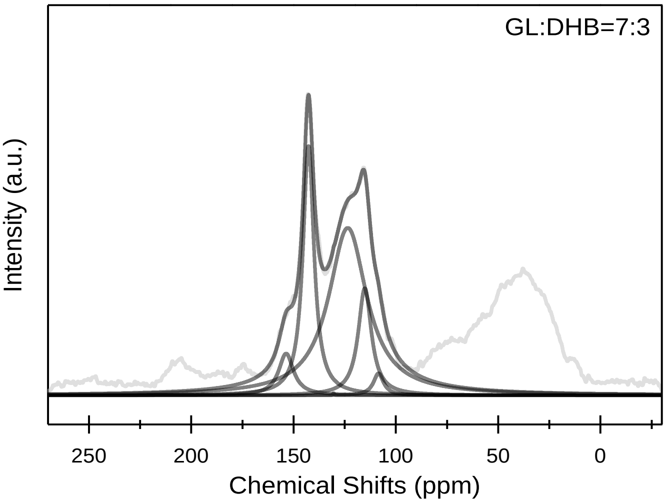

Figure 2-24. NMR spectrum of Co-CANP with Glucose to DHB ratio of 7:3 and its deconvolved peaks

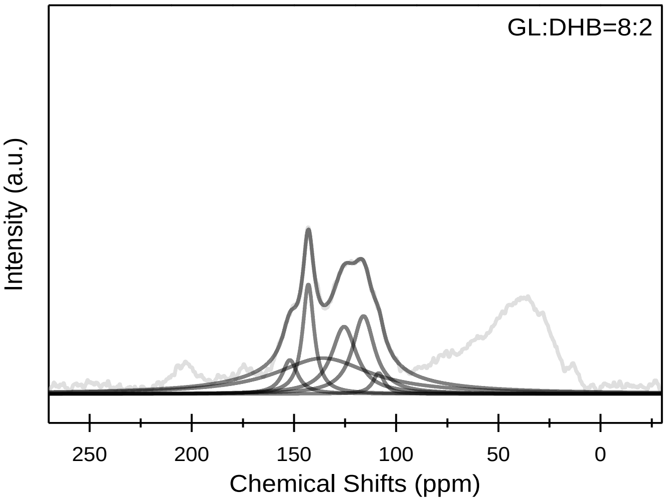

Figure 2-25. NMR spectrum of Co-CANP with Glucose to DHB ratio of 8:2 and its deconvolved peaks

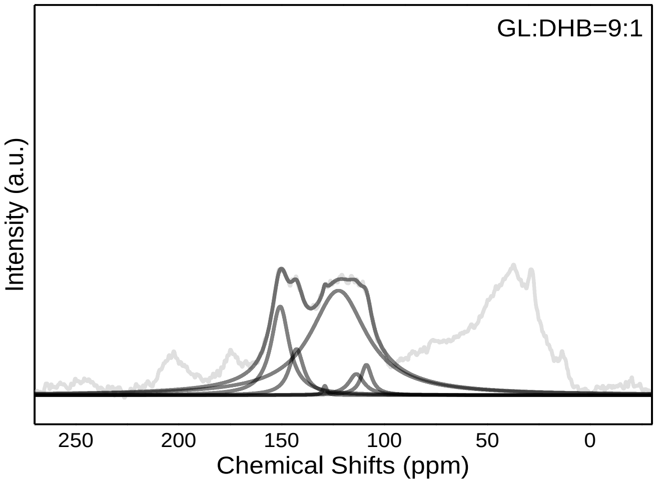

Figure 2-26. NMR spectrum of Co-CANP with Glucose to DHB ratio of 9:1 and its deconvolved peaks

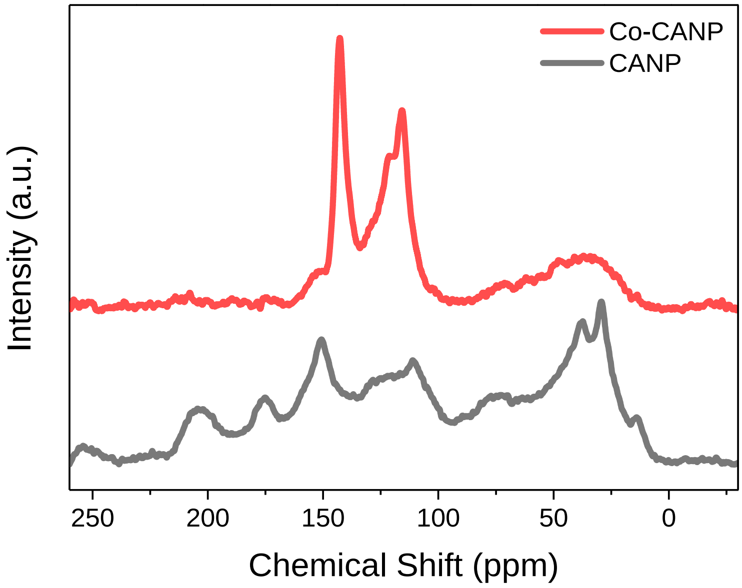

Figure 2-27. NMR spectra of Co-CANP and CANP

2.2.2.2 Fourier-transform infrared spectroscopy (FT-IR)

The Fourier transformation infra-red (FT-IR) spectra were used to inspect the functional group differences between Co-CANP and raw materials (glucose and DHB). Nicolet 6700 (Thermo Scientific) was used with ATR (attenuated total reflectance) mode in the range of 4000 to 650 cm^{-1}. The FT-IR spectra for glucose, DHB, and Co-CANP are given in Figure 2-28. Five zones appear in the FT-IR spectrum, where the peaks generated according to the carbon-carbon or carbon-oxygen bonding. The sharp peaks in the range of 700-1700 cm^{-1} in glucose and DHB become less apparent in the spectrum for Co-CANP, indicating removal of much of these functional groups due to the hydrothermal reactions. This can be regarded as evidence that dehydration occurred due to the reaction of glucose and DHB functional groups during hydrothermal process. In addition, shoulder peaks appearing in 3000-3600 cm^{-1} of Co-CANP show a different aspect from the raw material, which means that the chemical structure is changed by the reaction of glucose and DHB by thermochemical reaction. As mentioned earlier, a complete reaction does not occur when 60% of DHB is added, which can be seen from the FT-IR analysis in Figure 2-29.

Interestingly, changes in the FT-IR spectrum were observed depending on the powder size of Co-CANP ground by the pestle. The Co-CANP powder was prepared in three sizes, 75 μm or less, 75 ~ 100 μm, 100 ~ 200 μm of powder were prepared. As shown in Figure 2-30, the peaks appearing for the wavenumber are the same, but show differences in the intensity. Increased peak intensity of the FTIR spectrum generally means increased amount of functional groups per unit volume [31].

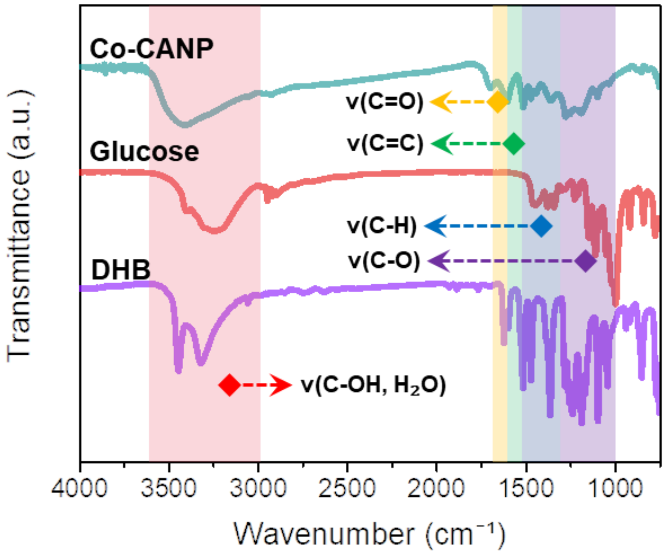

Figure 2-28. FT-IR spectra of Co-CANP, glucose, and DHB

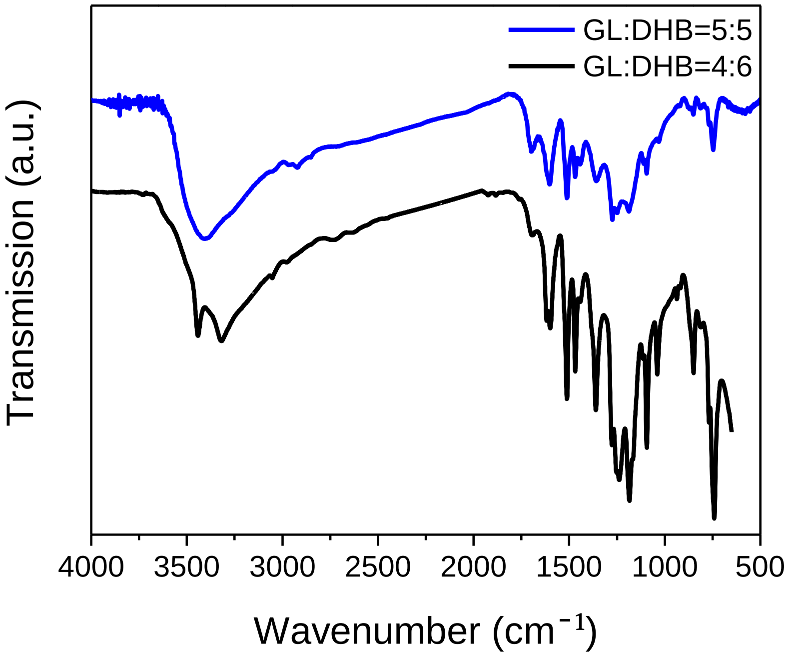

Figure 2-29. FT-IR spectra of Co-CANP according to the different glucose and DHB ratio.

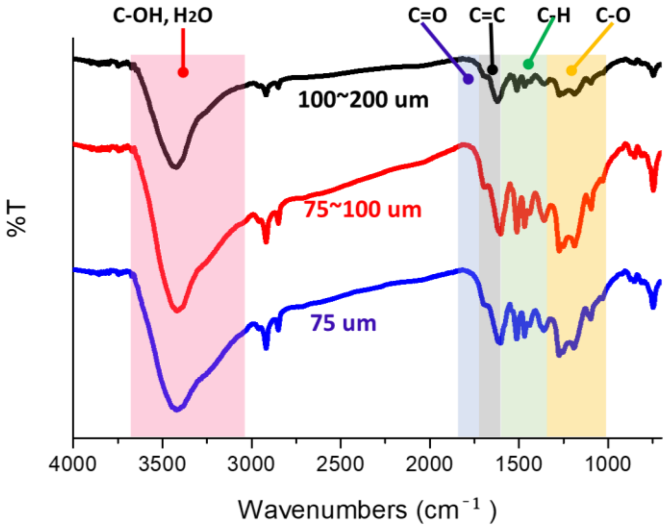

Figure 2-30. FT-IR Spectra according to powder size of Co-CANP

2.2.2.3 Raman spectroscopy

Raman spectroscopy is a non-destructive method of measuring chemical structure, molecular interaction, and crystallinity using light scattering. The Raman spectrum of Co-CANP was obtained using LabRAM HV Evolution (HORIBA) with a 532 nm laser. As shown in Figure 2-31, Co-CANP has two distinct peaks at 1371 cm^{-1} and 1588 cm^{-1}. In general, the peaks appearing near 1355 cm^{-1} and 1575 cm^{-1} are D peak and G peak, respectively [32]. Co-CANP has similar spectroscopic feature as graphene oxide, it has D peak at 1371 cm^{-1} and G peak at 1588 cm^{-1}. Therefore, Co-CANP, which shows D peak due to disorder band caused by the graphite edges and G peak due to graphitic lattice, also has graphitic features [32].

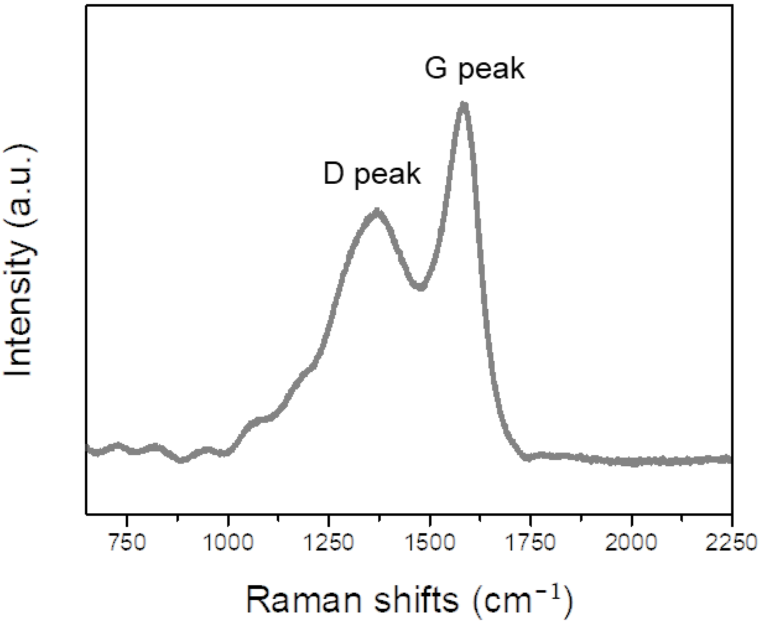

Figure 2-31. Raman spectrum of Co-CANP with D and G peaks

2.2.2.4 X-ray photoelectron spectroscopy (XPS)

XPS is efficient technique to measure elemental composition and chemical state. AXIS-His (KRATOS) was used for measuring chemical state of Co-CANP in the range of 0 to 1200 eV.

Figures 2-31 show the XPS spectra. In the wide range of binding energy, two peaks are appeared at 283 and 531 eV, those represent O1s and C1s [4, 33, 34]. Each peak is composed of various singular peaks, which can be identified by deconvolution. In figure 2-32(b) and (c), the original peak is given in gray and the deconvolved ones in color.

The convoluted peaks in Figure 2-32(b) represent sp^2 bonding and carbon bonding combined with oxygen functional groups. The peaks due to the carbon-oxygen bond appear in three places, two of them show peaks by C-O bonding, that is hydroxy groups, and the other indicate double bonding, that is carbonyl groups.

The deconvolved peaks in Figure 2-32(c) are related to oxygen 1s spectrum. This data shows information about the oxygen functional groups. Through deconvolved peaks in O1s region, it can be seen that the presence of oxygen functional groups in Co-CANP, mostly in the form of hydroxyl and carbonyl groups.

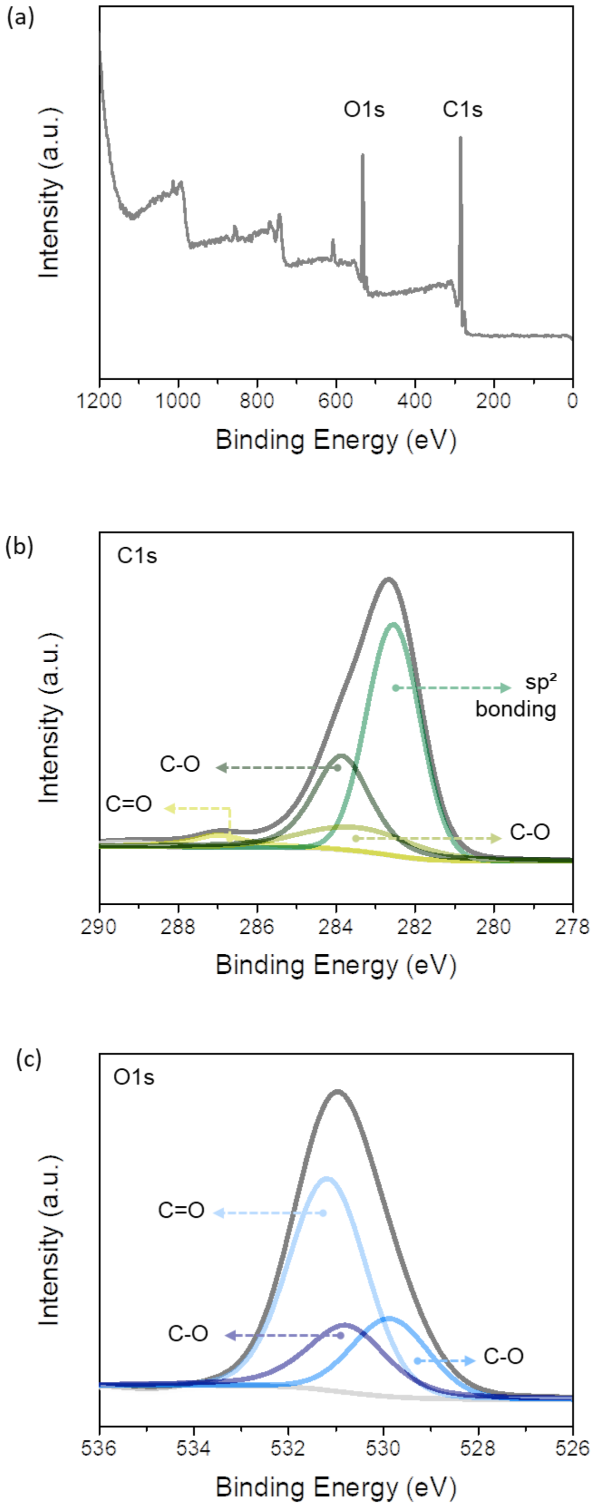

Figure 2-32. (a) XPS full spectrum of Co-CANP, (b) C1s, and (c) O1s spectrum

2.2.2.5 X-ray diffraction (XRD)

The inter-planar distance of the nanoplates can be calculated from X-ray diffraction (XRD) data according to Bragg's law. The 2D XRD, D8 Discover (Bruker) was utilized under these conditions; 0.15418 nm of X-ray wavelength and order of reflection (n) of 1. The measured XRD spectrum in Figure 2-33 has a peak at 20.13°. The calculated inter-planar distance of the Co-CANP is 0.44 nm. This value is smaller than that for graphene oxide (GO) for which the d-spacing is typically of 0.8 to 0.9 nm [35-37]. In the case of graphene, the inter-planar distance of graphene [36] becomes lager as the oxidation level increases, or with increasing oxygen functional groups on the surface of graphene. It can be deduced that the Co-CANP has a relatively small amounts of functional groups compared to GO.

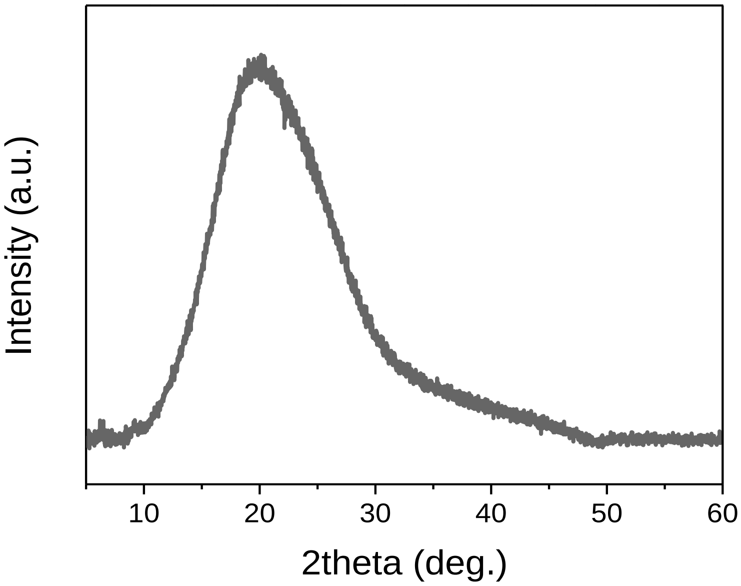

Figure 2-33. XRD spectrum with a peak at 20.13°

2.2.3 Thermal Gravimetry Analysis (TGA)

TGA is a method of observing the change in the weight characteristics of a material with temperature changes, it provides information of material about physical and chemical phenomena. The Discovery TGA (TA Instruments) under nitrogen filled condition from 40℃ to 900℃ with 10℃/min ramping rate. In Figure 2-34(a), a total weight loss of 54.6% occurred as the temperature was raised to 900°C. The two peaks in the derivative of the TGA curve occurs at 197.7°C and 407.9°C. It is known for GO that oxygen functional groups such as carbonyl, hydroxyl, carboxyl, and epoxy groups are removed in the range between 160°C and 370°C [38]. Thus, it can be construed that the first peak at 197.7°C indicates removal of oxygen functional groups attached to Co-CANP. For temperatures above 370°C, restructuring of carbon skeleton should occur [39].

In addition, another TGA experiment was also carried out under the atmospheric condition, and its results are shown in Figure 2-34(b). There are two distinct peaks in the range of 40-900°C, which occur at 176.3°C and 535°C, respectively. The overall weight loss was 99.21%, indicating that almost all Co-CANPs were oxidized and decomposed in high temperature region under atmospheric conditions.

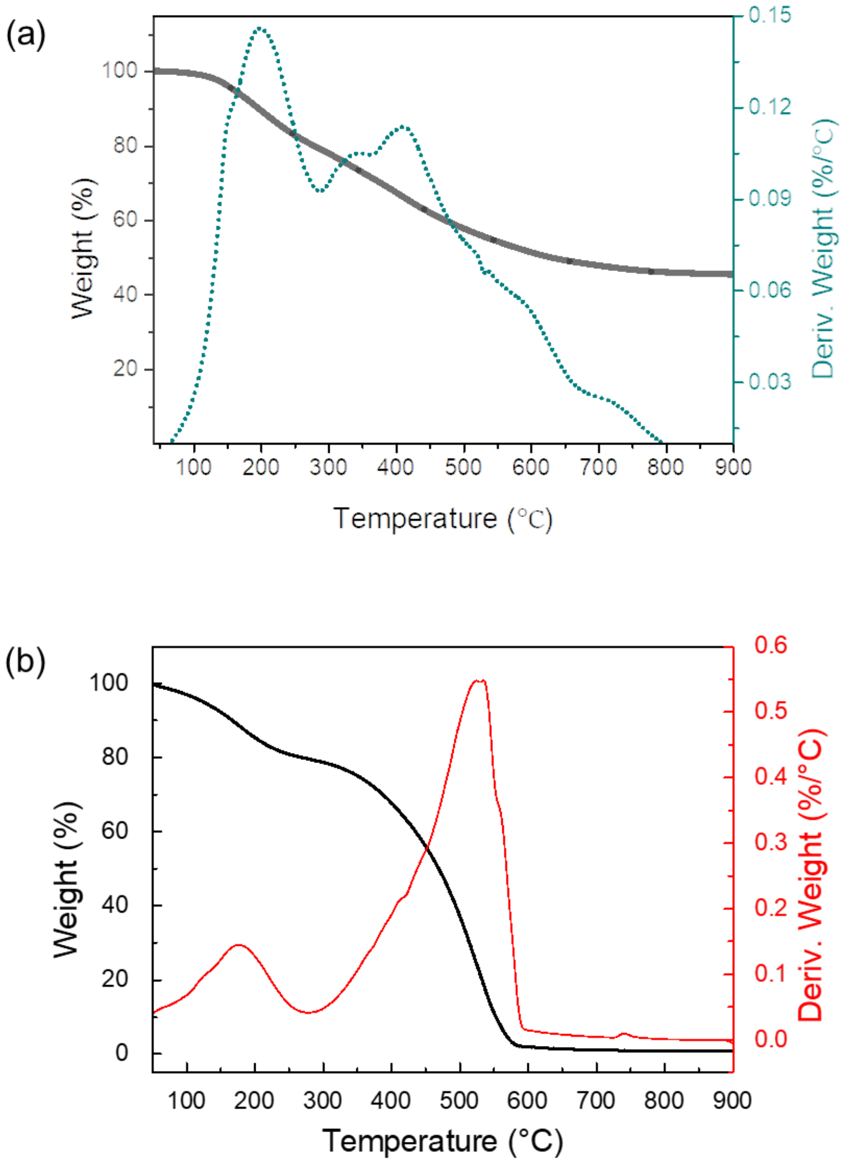

Figure 2-34. TGA spectrum of Co-CANP (a) under nitrogen atmosphere (b) under atmospheric condition

Chapter 3. Applications

3.1 Rubber composite for tire

Tires are indispensable for moving vehicles, and natural rubber and synthetic rubber are the main raw materials. Various chemical additives are added to achieve the desired performance. Among them, carbon black obtained after petroleum refining process plays an important role in increasing heat resistance, wear resistance, rigidity, and aging resistance by combining with rubber molecules [40-43]. However, carbon black obtained after petroleum refining process is not a good candidate in modern society trying to reduce petroleum oil consumption. Therefore, silica has been proposed and researched as an alternative of carbon black [43-45], but it has a disadvantage in that bonding strength with rubber molecules are poor, and wear resistance is not good enough [46].

To demonstrate the efficacy of Co-CANP, it was introduced to a rubber composite for tire as an additive. The tire composite was prepared by adding accelerators, antioxidants, vulcanizing agents, and bonding agents to rubber compound composite of solution styrene butadiene rubber (S-SBR) and neodymium butadiene rubber (Nd-BR). To prepare tire composite, S-SBR, Nd-BR, treated distillate aromatic extract (TDAE) oil, silica, coupling agent, zinc oxide, stearic acid, N-(1,3-dimethylbutyl)-N’-phenyl-p- phenylenediamine (6PPD), poly(1,2-dihydro-2,2,4-trimethyl-quinoline) (TMQ), general wax, and 1,3-Diphenylguanidine (DPG) were used. Figure 3-1 is an optical image of final product of tire composite. Figures 3-2(a) through (c) show the surface of the composite without the Co-CANP and Figure 3-2(d) through (f) the surface with 0.5 wt% of Co-CANP added. The surface of the composite becomes rougher with the presence of the Co-CANP.

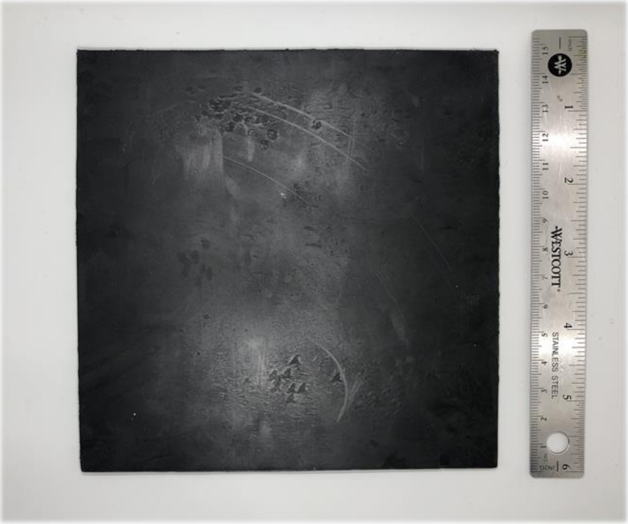

Figure 3-1. As prepared 0.5 wt% of Co-CANP added rubber compound composite

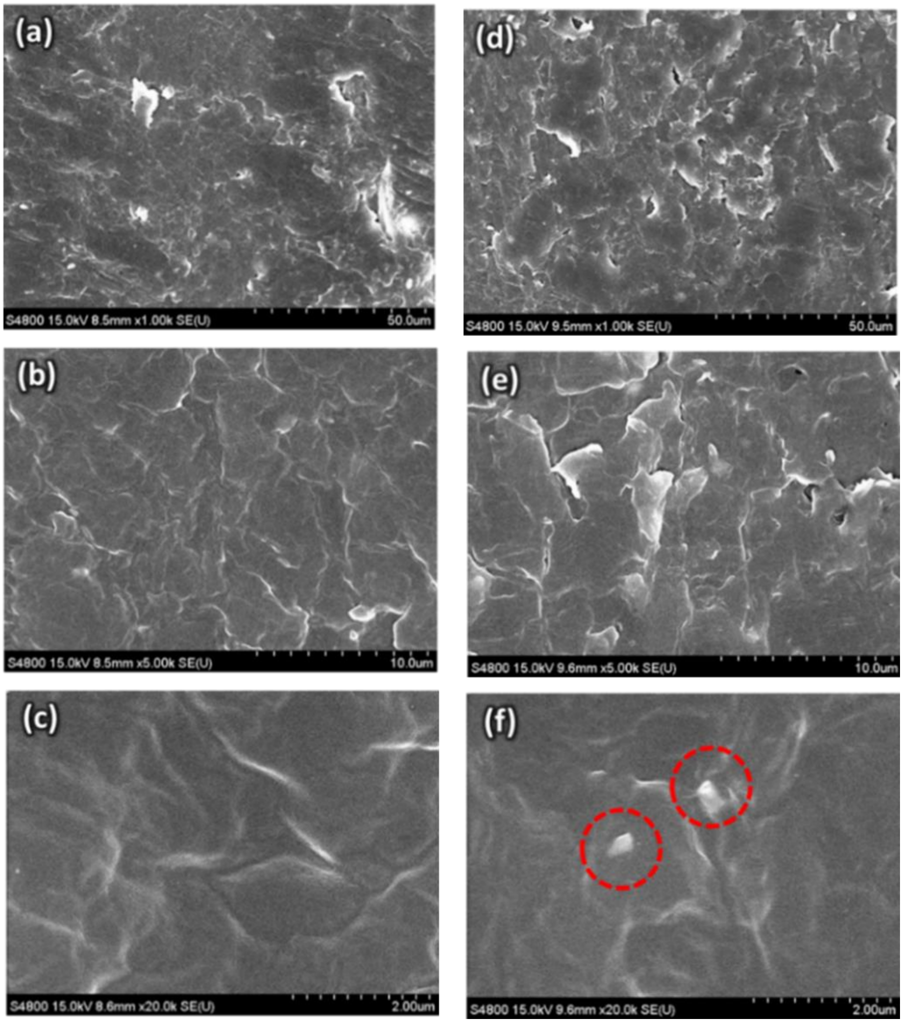

Figure 3-2. SEM images of S-SBR composites (a-c) composites without fillers (d-f) composites with 0.5 wt% of Co-CANPs as fillers. Red circles are indication of Co-CANPs

3.1.1 Mechanical tensile test

Experiments were conducted to evaluate the mechanical performance of the composite. Tensile test results are shown in Figure 3-3 for the tire composite with the additive at the level of 0.5 wt%. To compare reinforcement performance, both CANP (using only glucose as raw material) and Co-CANP (using glucose and DHB as raw material) were utilized as an additive. Comparing the composites containing 0.5 wt% of additive with the reference sample in Figure 3-3, the elongation to failure remains the same for all but the tensile strength increased with the introduction of the additives. The tensile strength enhancement for CANP is only 3.2%, but it is 29.4% for Co-CANP (from 16.35 MPa to 21.15 MPa).

In order to investigate the performance improvement of the tire composite material according to the loading amounts of Co-CANP, additional tensile test was conducted for composite material added with 0.5 wt%, 1 wt%, 2wt% of Co-CANP as a filler. The samples have their respective references, the tensile results for 3 different samples are shown in Figure 3-4. Tensile strength increased only in samples with 0.5 wt% of Co-CANP added as a filler, and decreased in the 1 wt% and 2 wt%. Elongation increased both 0.5 wt% and 1 wt% sample, but slight decreased in the 2 wt% sample. In summary, the sample with a tendency to increase both tensile strength and elongation is when 0.5 wt% of Co-CANP added. Thus, it can be concluded that the optimal filler amount to increase the mechanical properties is 0.5 wt%.

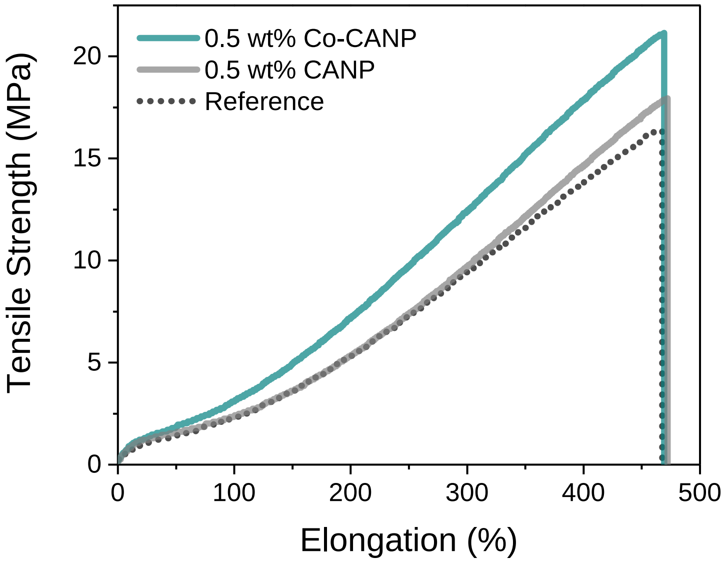

Figure 3-3. Tensile strength versus elongation data from tensile test

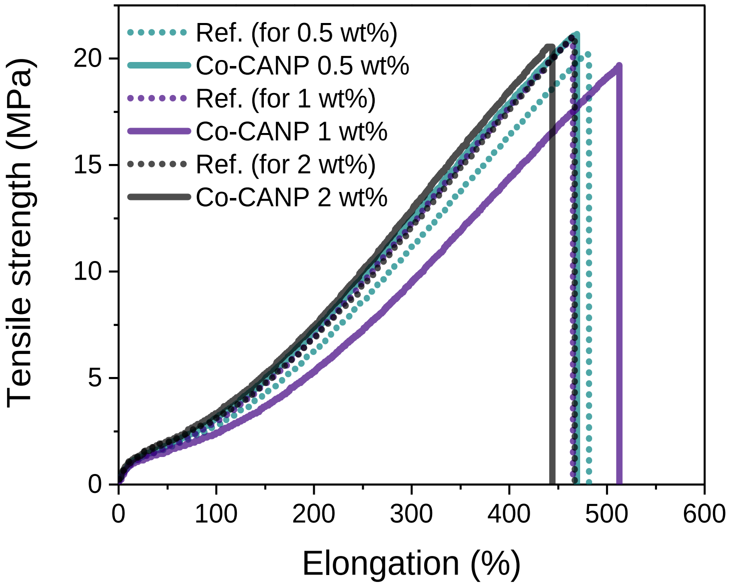

Figure 3-4. Tensile test results of different composition ratio of Co-CANP

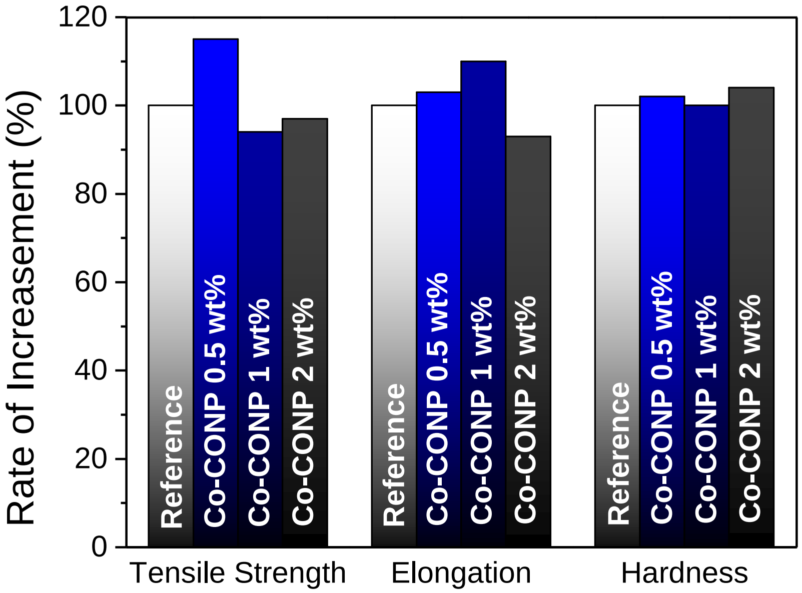

Figure 3-5. Comparison of increasement rate for tensile strength, elongation and hardness

3.1.2 Dynamic mechanical analysis (DMA)

Viscoelastic behavior of composites is often evaluated by dynamic mechanical analysis techniques. Important tire performances, rolling resistance and wet traction, can be evaluated by DMA. Rolling resistance and wet traction are considered as properties to assess tire performance. Rolling resistance means that the tire easily rolls on the road without resistance. If this value is large, energy loss due to exothermic reaction occurs. In addition, wet traction is considered as an important factor for safety because it indicates the degree of traction and braking force exerted on wet road surface.

DMA was conducted in tension mode to evaluate the rolling resistance and wet traction characteristics of the tire using Seiko Exstar 6000 (DMA/SS6100) (SEICO) under nitrofen filled condition in the temperature range of -80 to 80°C with 5°C/min ramping rate. The storage modulus (E'), representing elastic behavior, can be obtained by measuring stored energy in composite. The loss modulus (E''), representing viscous behavior, can be measured by dissipated energy as heat. Both dynamic moduli have following equations;

$$\mathrm{E}' = \frac{\sigma_0}{\varepsilon_0} cos\delta$$

$$\mathrm{E}'' = \frac{\sigma_0}{\varepsilon_0} sin\delta$$

As shown in Figure xx, DMA results are shown for two composite samples when 0.5 wt% Co-CANP and CANP was added as fillers. In case of 0.5 wt%

of Co-CANP added, the storage modulus is increased in the sub-zero temperature range. On the other hand, there was no increase or decrease when using CANP. There was a significant difference in loss modulus between the CANP added composite and the Co-CANP added composite. In the sub-zero temperature range, CANP added samples show a decrease in loss modulus, whereas Co-CANP samples have lower loss modulus values than the reference below -50°C and then suddenly increase from -50°C.

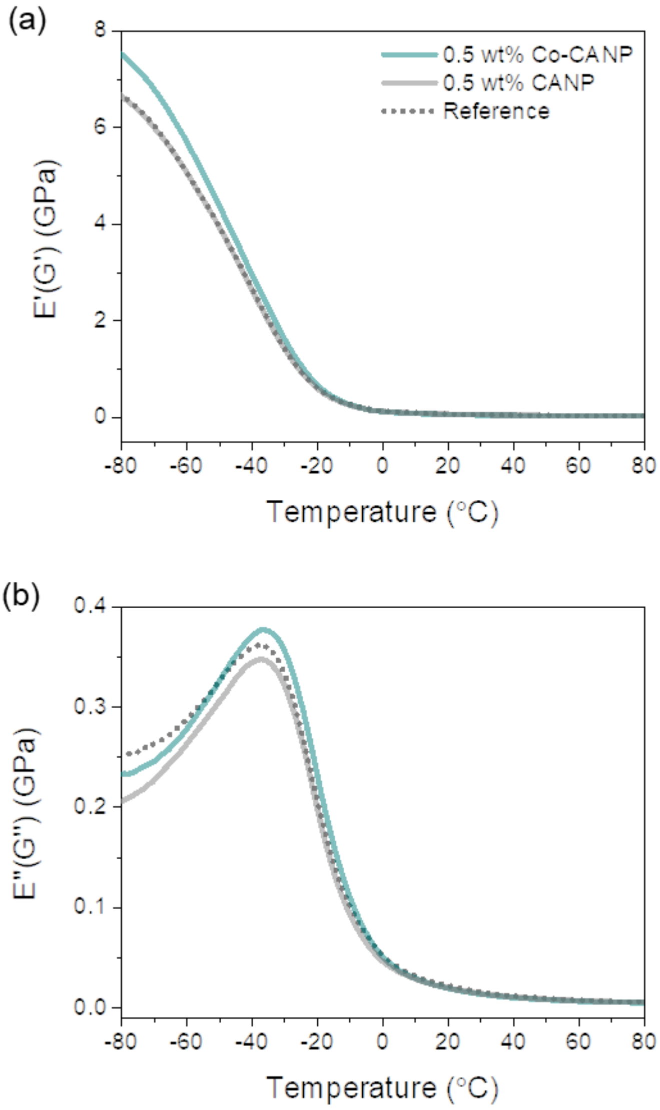

Figure 3-6. a) Storage modulus b) Loss modulus from DMA test results of tire composites with no filler (Reference), 0.5 wt% Co-CANP (synthesized from mixture of glucose and DHB), and 0.5 wt% CANP (synthesized from glucose only)

Both moduli are used for calculating tan δ. The ratio of loss to storage modulus are defined as $\tan\delta$. This is an indicator of damping in the material.

$$\tan\delta = \frac{E''}{E'}$$

Figure 3-7 gives the damping factor (tan δ) obtained from DMA test in the range of -80°C to 80°C. The tan δ at 60°C is used as an index of rolling resistance [47, 48]. The figure shows that there is little difference in the resistance regardless of the presence of the additive. However, there are certain improvements in the tan δ at 0°C, which is the wet traction performance indicator [48]. The composite material with Co-CANP added has the highest wet traction value (tan δ=0.40), compared to the reference sample without any additive (tan δ=0.37) and the composite with CANP (tan δ=0.35). Thus, the addition of CANP deteriorates rather than improves the wet traction. These results clearly illustrate the advantages that can be gained by co-compounding CANP with another compound.

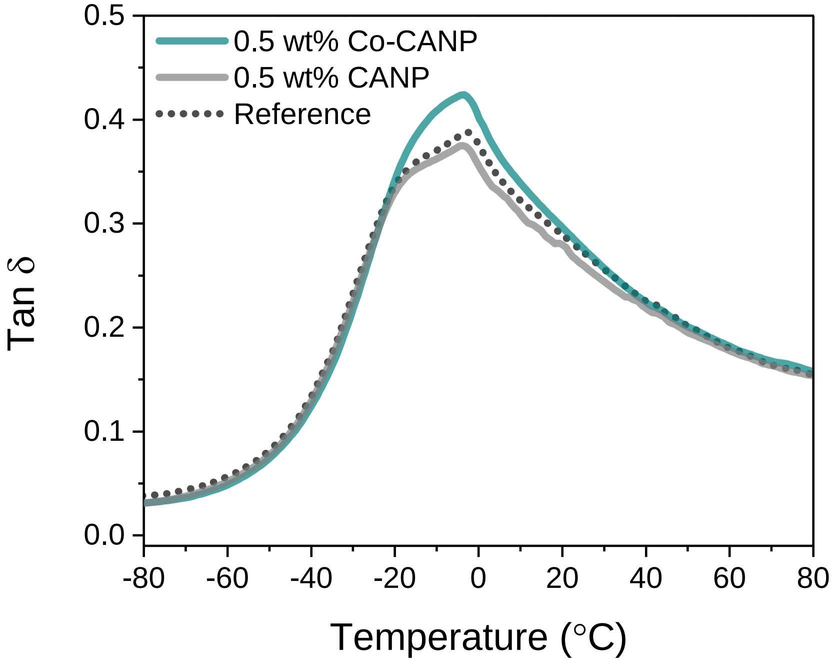

Figure 3-7. Tanδ from DMA test result of tire composites with no filler (Reference), 0.5 wt% Co-CANP and 0.5 wt% CANP

3.2 Sound absorption material

Sensory pollution caused by light, noise, and odor is one of the factors that harm the mental and physical health of modern people. Among them, pollution caused by noise is a frequent problem in densely populated cities, causing conflict between neighbors and becoming a serious social problem. In order to solve this problem, studies on sound absorbing materials have been actively conducted. Commercially available sound absorbing materials are classified into two types, one is a sound absorbing material by resonance and the other is a porous sound absorbing material [49, 50]. Resonant absorption materials show high absorption in the low frequency range, but its main disadvantage is that the absorbable frequency band is narrow [51] .

In the case of porous sound absorbing materials, excellent sound absorption performance in a wide frequency range and their light weight are great advantages [51]. Fibrous materials and porous foams are mainly used as sound absorbing materials.

When sound waves strike porous materials, the incident sound waves are consumed by conversion into mechanical and thermal energy in the porous material; this means that energy is absorbed by the material. The remaining energy, which is not consumed in material, is released by reflection and transmittance as shown in Figure 3-8(a) [52].

This is represented by the following equation;

$$E_i = E_R + E_A + E_T$$

Where E_i is incident energy, E_R is reflected energy, E_A is absorbed energy, and E_T is transmitted energy.

Sound absorption coefficient (α) is an index indicating sound absorption performance and is calculated as follows.

$$\alpha = 1 - \frac{E_R + E_T}{E_i} = \frac{E_a}{E_i}$$

An effective method of improving sound absorption performance is to make structural changes in the sound absorbing material. Sound absorption material with tortuous path consumes larger energy than sound absorber having simple structure as shown in figure 3-8(b). In addition, when the incident waves contact area increases, the absorbed energy is increased. Recent study about sound absorption performance also says that semi-open cell which is randomly blocked by graphene oxide nanosheets has superior sound absorption property as shown in Figure 3-9 [53].

Accordingly, Co-CANP was added as a filler to porous foam to enhance sound absorption performance. Commercially available melamine foam was used as the base material and various loading amounts of Co-CANP was added.

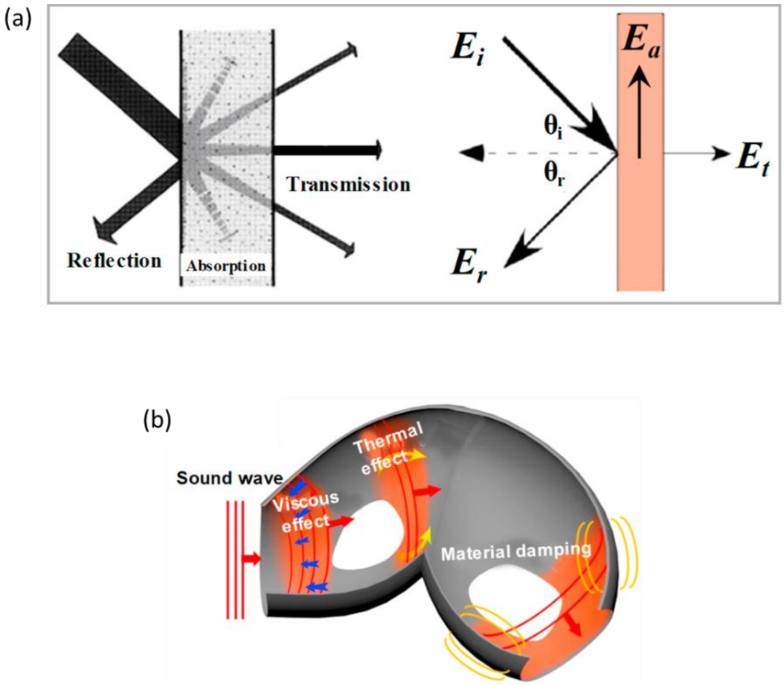

Figure 3-8. (a) Schematic of the sound absorption process for porous materials [52] (b) Schematic diagram showing the energy consumption mechanisms of porous sound absorption materials [54].

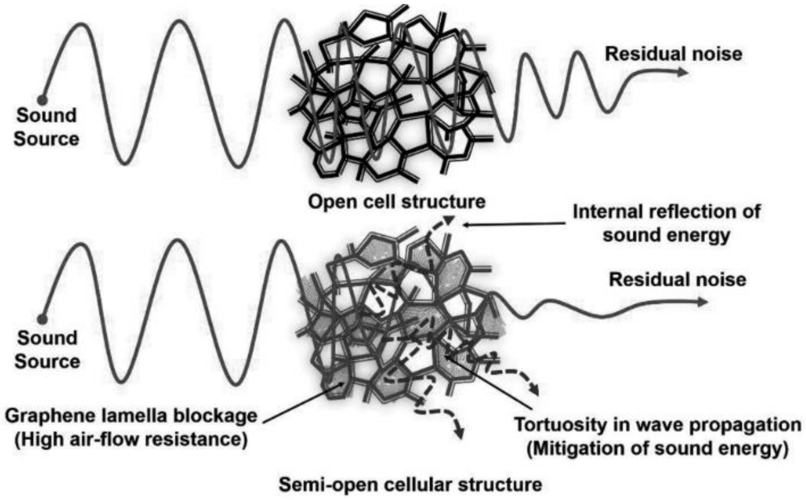

Figure 3-9. Schematic of acoustic propagation through lamella structures [53]

3.2.1 Co-CANP/Melamine hybrid foam

Co-CANP/Melamine (ML) hybrid foam was fabricated via dip coating method. In this study, commercially available melamine foam from BASF was used, and Co-CANP was synthesize by vapor-filled hydrothermal method. Simple schematic image is depicted in Figure 3-10. Before dip coating process, melamine foam was cut into cylindrical shape having diameter of 29 mm. To fabricate Co-CANP/ML hybrid foam, melamine foam was soaked in Co-CANP solution dispersed in DMF, and the concentration of Co-CANP solution was 1, 2.5, 5, 7.5, and 10 mg/ml. And then, it was fully dried on an 80°C hotplate for overnight. This process was repeated five times to obtain a final product (Figure 3-11). The Co-CANP coated melamine foam was washed using DI water, and then finally dried in oven at 80°C. Pristine melamine foam has 10.37 kg/m^3, and foams with different densities were made according to the concentration of the solution as shown in figure xx. The inner structure of fabricated Co-CANP/ML hybrid foam was investigated using SEM as shown in Figure 3-13. Melamine foam has a porous structure, and its pore size is several hundred micrometers. The higher the concentration of CO-CANP solution, the higher density of the hybrid foam was made. As the density increases, the amount of coated Co-CANP increases. However, the amount of Co-CANP coated on the outside and inside of the melamine foam is different (Figure 3-12 and 3-13), which means that the Co-CANP did not effectively penetrate into the bulk melamine foam.

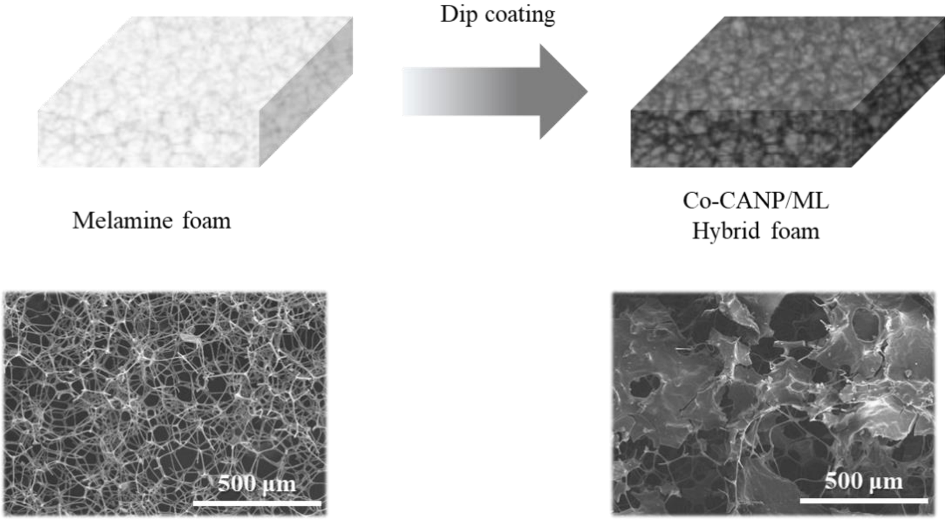

Figure 3-10. Schematic diagram of manufacturing process of Co-CANP/ML hybrid foam, and SEM image of internal structure of foams

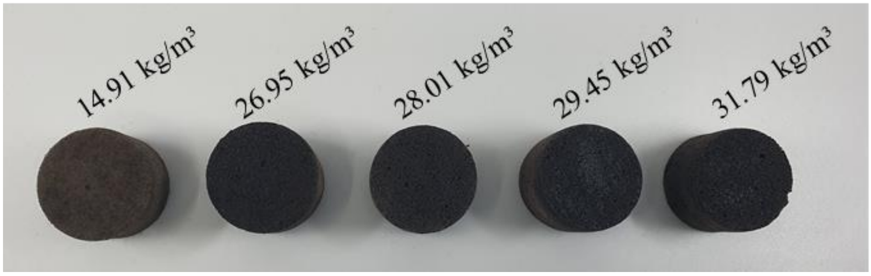

Figure 3-11. Optical image of foams with different densities according to the amount of Co-CANP added

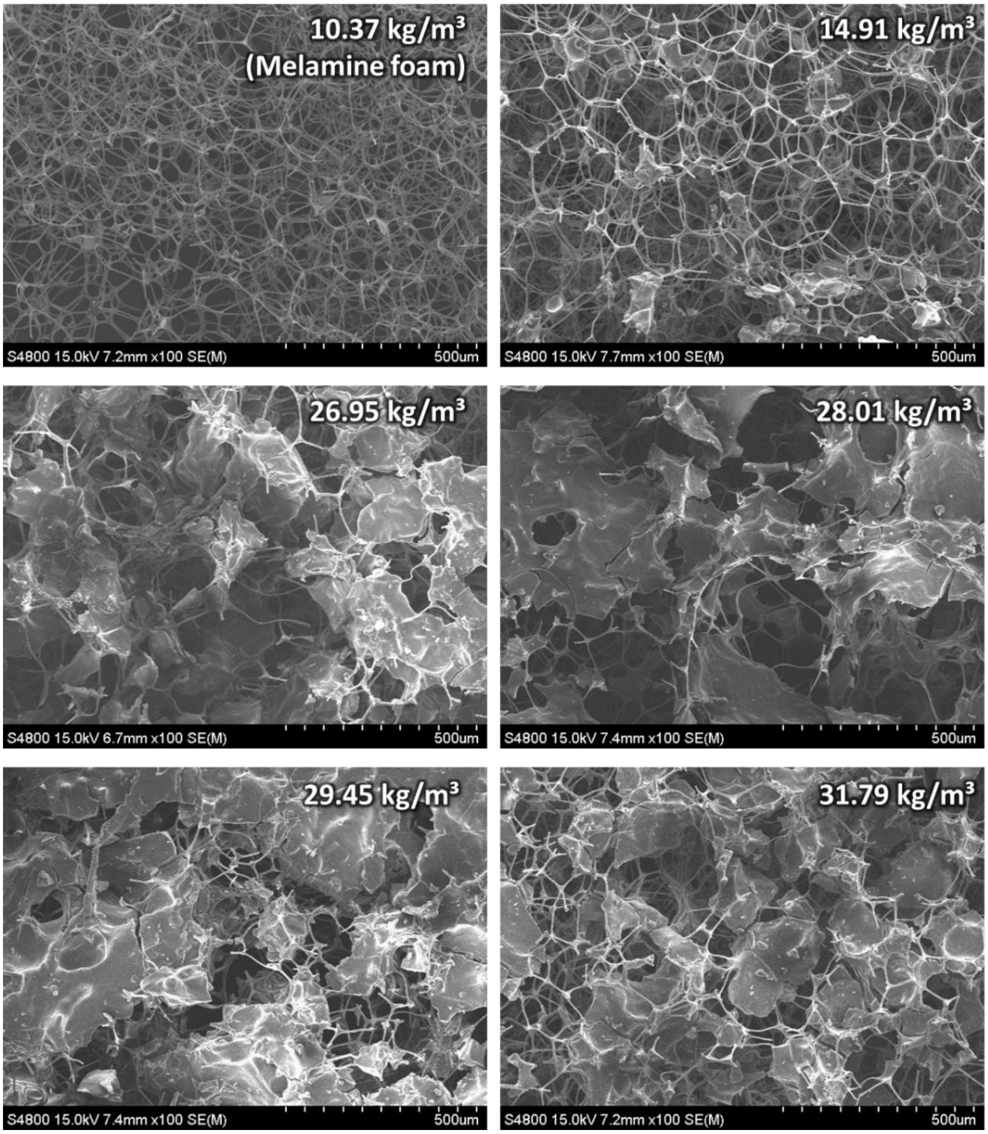

Figure 3-12. SEM images of outer side of Co-CANP/ML hybrid foams

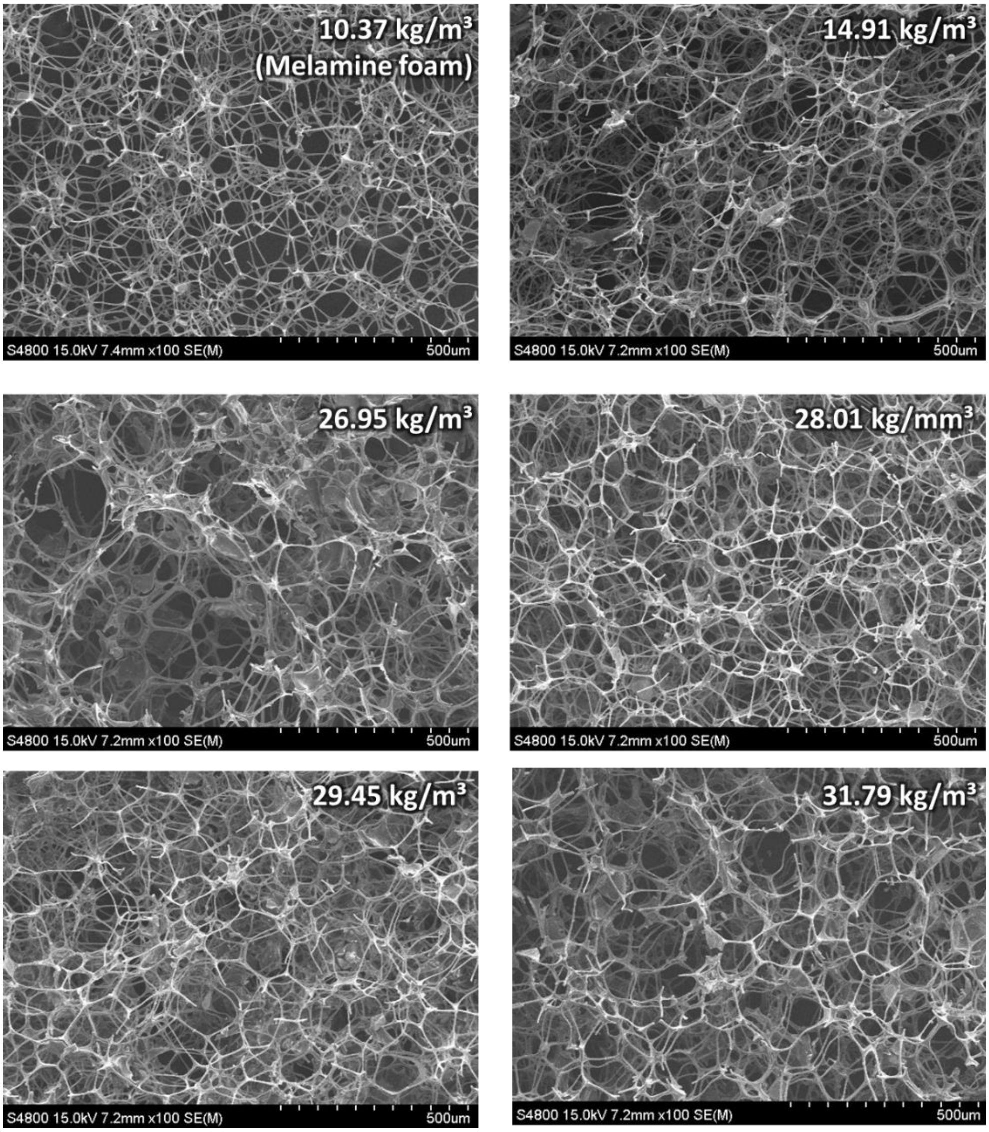

Figure 3-13. SEM images of inner side of Co-CANP/ML hybrid foam

3.2.2 Sound absorption coefficient

The measurement of sound absorption performance for Co-CANP/ML hybrid foam was conducted using B&K 4206 impedance tube. All experiments were conducted in the range of 50 Hz to 6.3 kHz, and foams having a thickness of 20 mm were used. We measured six samples with different density from 10.37 to 31.79 kg/m^3. Figure 3-14 to 3-19 shows the sound absorption coefficient measured using an impedance tube. All samples with Co-CANP added to melamine foam show an increase in sound absorption coefficient between 1500 and 5000 Hz.

Based on the measured sound absorption coefficient, the normalized value over the measured frequency can be obtained. This is called normalized sound coefficient. The normalized sound coefficient (α_n) which stands for acoustic activity can be calculated using below equation [55].

$$\alpha_n = \frac{\int_{f_1}^{f_2} \alpha(f)df}{f_2 - f_1}$$

Based on the calculated data, the sound absorption coefficient increased by nearly 10% in the 31.79 kg/m^3 sample. Through this, it can be seen that Co-CANP, a two-dimensional nanoplate, directly affects the sound absorption performance. This means that when the sound waves reach Co-CANP, it is converted into thermal energy by micro-vibration. As more Co-CANP is added, a larger increase in sound absorption performance can be predicted.

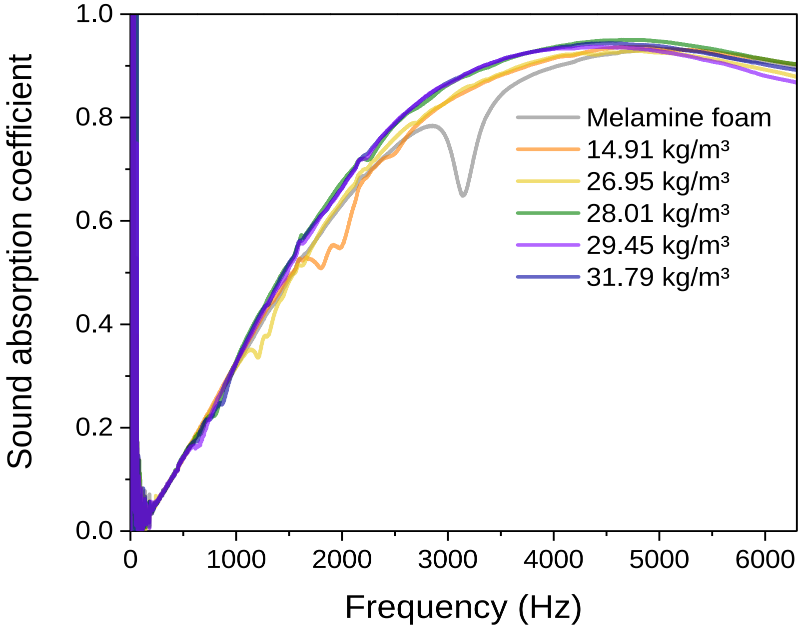

Figure 3-14. Sound absorption coefficient of Co-CANP/ML hybrid foams as compared to pristine melamine foam

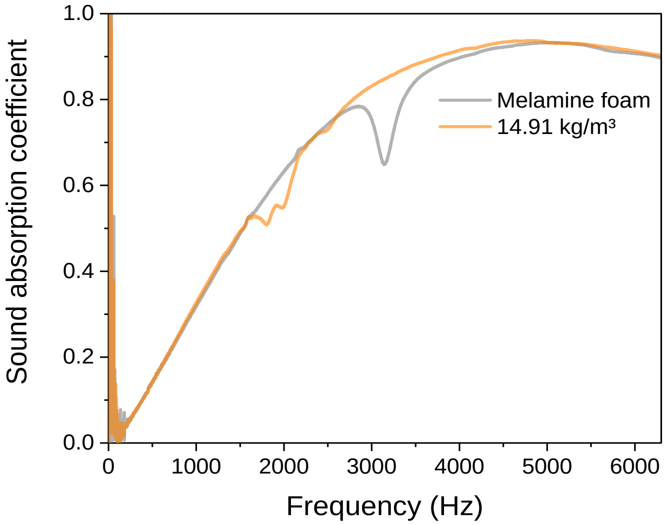

Figure 3-15. Sound absorption coefficient of Co-CANP/ML hybrid foam with a density of 14.91 kg/m^3

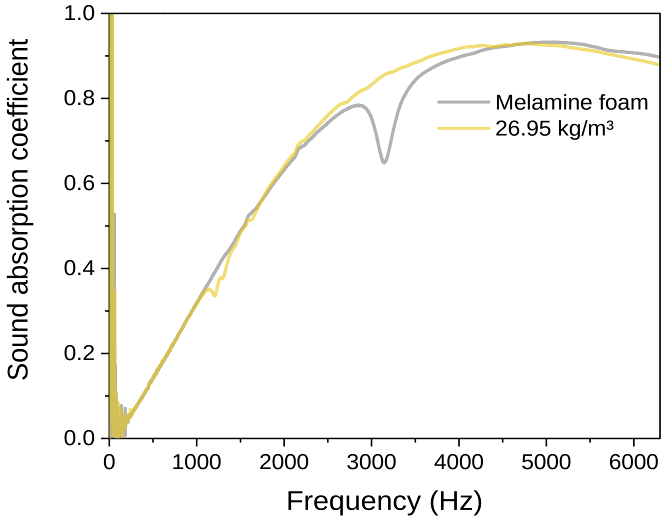

Figure 3-16. Sound absorption coefficient of Co-CANP/ML hybrid foam with a density of 26.95 kg/m^3

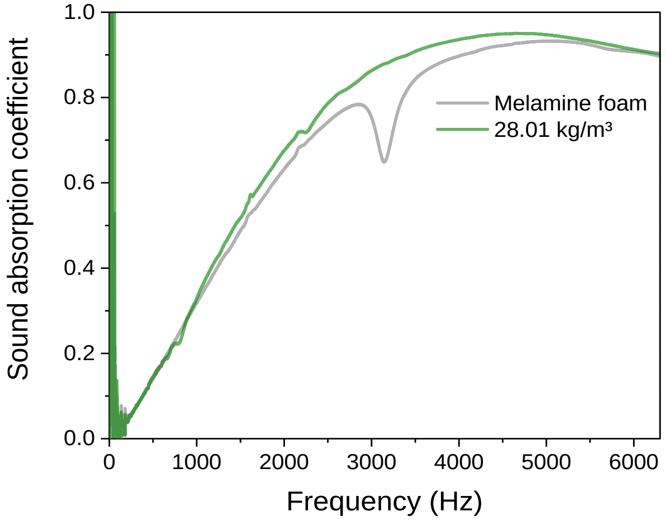

Figure 3-17. Sound absorption coefficient of Co-CANP/ML hybrid foam with a density of 28.01 kg/m^3

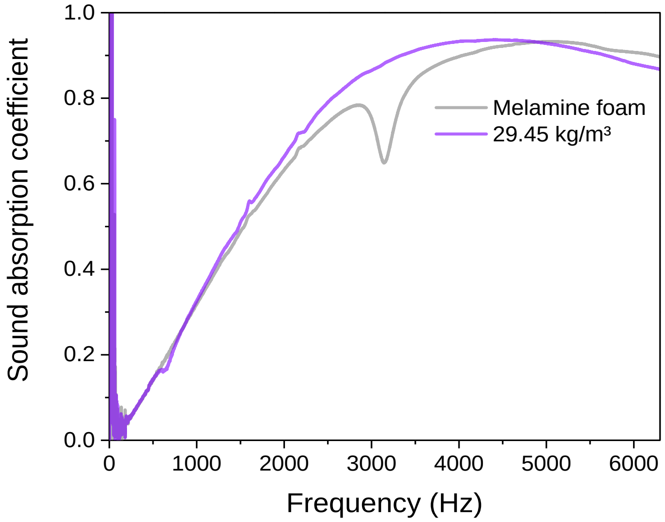

Figure 3-18. Sound absorption coefficient of Co-CANP/ML hybrid foam with a density of 29.45 kg/m^3

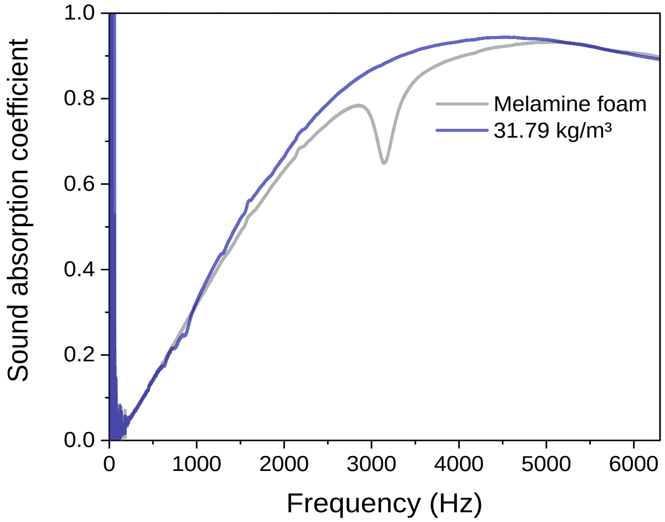

Figure 3-19. Sound absorption coefficient of Co-CANP/ML hybrid foam with a density of 31.79 kg/m^3

	50 Hz – 6.3 kHz	
Density [kg/m³]	Normalized sound absorption coefficient (α_n)	Increasement
10.37	0.706	100.0
14.91	0.695	98.5
26.95	0.698	98.9
28.01	0.720	102.0
29.45	0.716	101.5
31.79	0.776	109.9

Table 2. Normalized sound absorption coefficient with different density of Co-CANP/ML hybrid foams

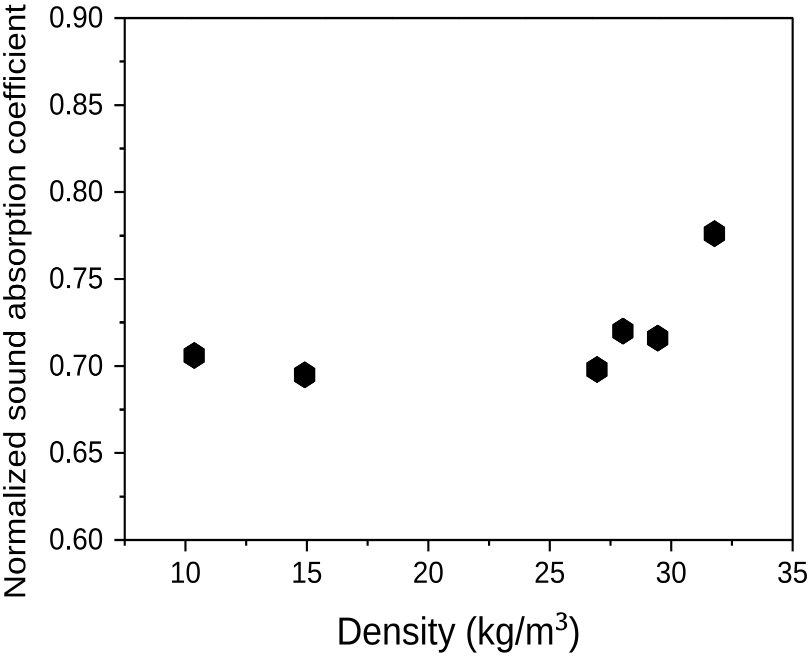

Figure 3-20. Plotting of normalized sound absorption coefficient according to the density of Co-CANP/ML hybrid foams

To compare sound absorption coefficient more practically, the sound absorption coefficients at 500, 1000, 2000 and 4000 Hz in 1/3 octave bands, were compared measured sound absorption coefficient with the commercial acoustic absorbers [53, 56-58]as shown in table 3.

Materials	Density [kg/m^3]	Thicknes [mm]	Sound absorption coefficient			
			500 Hz	1000 Hz	2000 Hz	4000 Hz
Polyurethane foam	37.4	40	0.06	0.84	0.15	0.21
Aluminum foam	9320	20	0.13	0.22	0.52	-
Wood	-	16	0.1	0.09	0.08	0.07
Cocos fiber roll felt	-	29	0.22	0.35	0.47	0.57
Acoustical plaster	350	25	0.66	0.65	0.62	0.68
Rock wool	80	50	0.92	0.9	0.88	0.88
Mineral wool	70	50	0.65	0.6	0.75	0.65
Perforated veneered chipboard	-	50	0.58	0.59	0.68	0.35
Natural coir fiber	153	30	0.28	0.84	0.73	0.82
Melamine foam	10.37	20	0.141	0.317	0.632	0.897
Co-CANP/ML hybrid foam	14.91	20	0.144	0.326	0.551	0.915
	26.95	20	0.141	0.316	0.64	0.917
	28.01	20	0.145	0.328	0.675	0.936
	29.45	20	0.141	0.325	0.662	0.933
	31.79	20	0.143	0.324	0.663	0.933

Table 3. Comparison of sound absorption coefficient for various commercial sound absorbers and Co-CANP/ML hybrid foams in 1/3 octave bands

3.3 Heat dissipation material

As the circuits of electronic devices become highly integrated, more heat is generated from the components. Failure of releasing the generated heat in a timely manner will result in deformation of the components and mechanical failure [59-62]. Accordingly, heat dissipation components are considered as essential and important elements in electronic devices [63]. In the past, metallic materials with high thermal conductivity were used, but the heavy weight and the limitation of heat dissipation performance raised the need for new heat dissipating materials [64-66]. Therefore, lightweight materials with improved heat dissipation performance have been utilized for efficient heat dissipation [64, 65, 67-71]. These studies have demonstrated that heat sinks based on nanomaterials [67, 68], especially low dimensional nanocarbon materials [64, 69, 71], have improved heat dissipation efficiency as shown in figure 3-21, 22. Since nanocarbon materials with sp^2 bonding have significantly higher thermal conductivity than sp^3 bonding and amorphous carbon[26], Co-CANP with sp^2 bonding is expected to have high thermal conductivity.

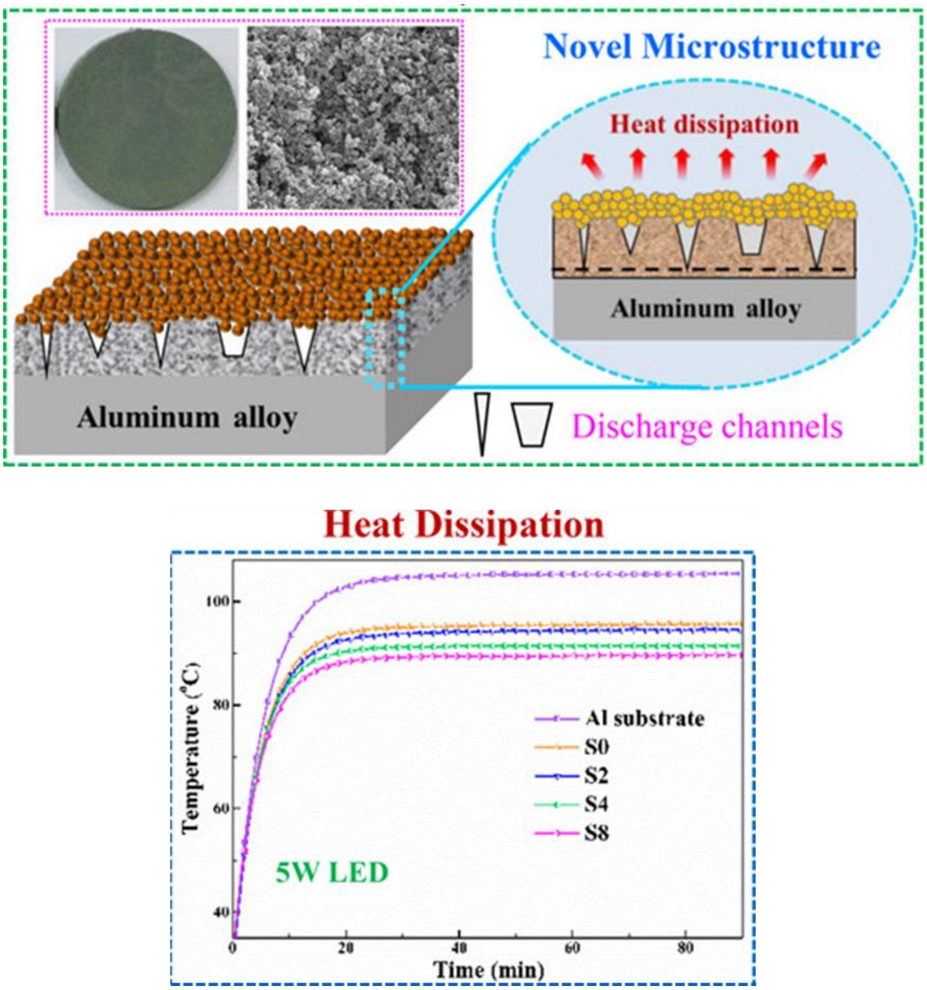

Figure 3-21. schematic structure of nanocomposite coating and its passive heat dissipation performance [68].

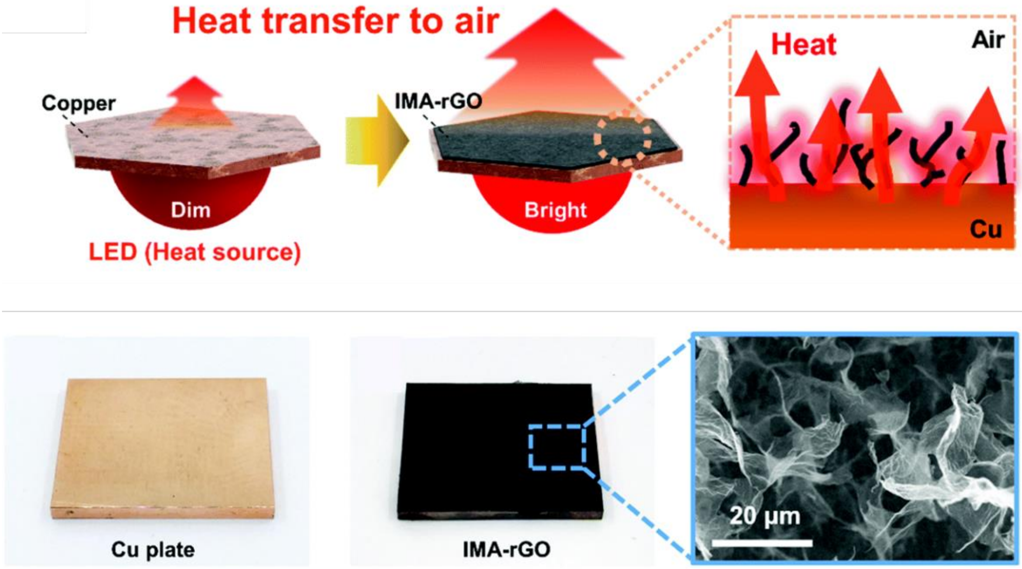

Figure 3-22. Schematic illustration of heat dissipation through IMA-rGO on copper heat sink. Optical images of copper plate before and after IMA-rGO plating. Magnified image by scanning electron microscopy (SEM) of IMA-rGO coated on copper plate [64].

Heat transfer occurs in three ways; convection, conduction and radiation [72]. To increase heat transfer by convection, it is desirable to maximize the surface area of the heat dissipating material according to following equation:

$$q_{conv} = hA(T_s - T_\infty)$$

Where q_{conv} is heat transfer rate by convection, h is heat transfer coefficient, A is area, T_s is surface temperature of heat sink, and T_∞ is temperature of environmental fluid [73]. Therefore, it is a very reasonable idea to increase the amount of heat released by convection by maximizing the surface area using nanomaterials, which can be confirmed by the above equation.

Thermal radiation in which heat energy is converted into electromagnetic energy is highly related to the material properties and surface area. The amount of heat released by thermal radiation is determined by the following equation :

$$q_{rad} = \frac{\sigma}{\left(\frac{1}{\epsilon_2} + \frac{A_2}{A_1}\left(\frac{1}{\epsilon_1} - 1\right)\right)} A_2({T_s}^4 - {T_a}^4)$$

where σ is a Stefan-Boltzmann constant=5.67×10^{-8}W $m^{-2}K^{-4}$, and A_1, ϵ_1, T_a each stand for surface area, thermal emissivity, temperature of surrounding air. A_2, ϵ_2, T_s are surface area, thermal emissivity, temperature of heat source. When $A_2 \ll A_1$, the formula for heat release by radiation can be simplified as follows:

$$q_{rad} = \sigma\epsilon_2 A_2({T_s}^4 - {T_a}^4)$$

It can be used to spread heat in infinite space. According to the above simplified equation, the use of materials with high thermal emissivity and high surface area can increase the amount of heat released by radiation. The thermal emissivity has a value from 0 to 1, and the closer to 1, the more similar to black body. The thermal emissivity values of the materials are given in Table 4 [74-76].

Material	Emissivity Coefficient	Material	Emissivity Coefficient
Blackbody	1.00	Green leaves	0.88
Cavity radiator	0.99-1.00	Ice	0.96
Aluminum (anodized)	0.70	Iron or steel (rusted)	0.70
Aluminum (oxidized)	0.11	Nickel (oxidized)	0.40
Aluminum (polished)	0.05	Nickel (unoxidized)	0.04
Aluminum (rough surface)	0.06-0.07	Nichrome (80Ni-20Cr) (oxidized)	0.97
Asbestos	0.96	Nichrome (80Ni-20Cr) (polished)	0.87
Brass (dull tarnished)	0.61	Oil	0.80
Brass (polished)	0.05	Silicon	0.64
Brick	0.90	Silicone rubber	0.94
Bronze (polished)	0.10	Silber (polished)	0.02
Carbon-filled latex paint	0.96	Skin (human)	0.93-0.96
Carbon lamp black	0.96	Snow	0.85
Chromium (polished)	0.10	Soil	0.90
Copper (oxidized)	0.6-0.7	Stainless steel (buffed)	0.20
Copper (polished)	0.02	Steel (flat rough surface)	0.95-0.98
Cotton cloth	0.80	Steel (ground)	0.56
Epoxy resin	0.95	Tin plate	0.10
Glass	0.95	Water	0.96
Gold	0.02	White paper	0.92
Gold-black	0.98-0.99	Wood	0.93
Graphite	0.7-0.8	Zinc (polished)	0.04

Table 4. Emissivity coefficient of various materials

It is assumed that there is no heat dissipation by conduction in general heat dissipating material, and description thereof will be omitted as shown in Figure 3-23.

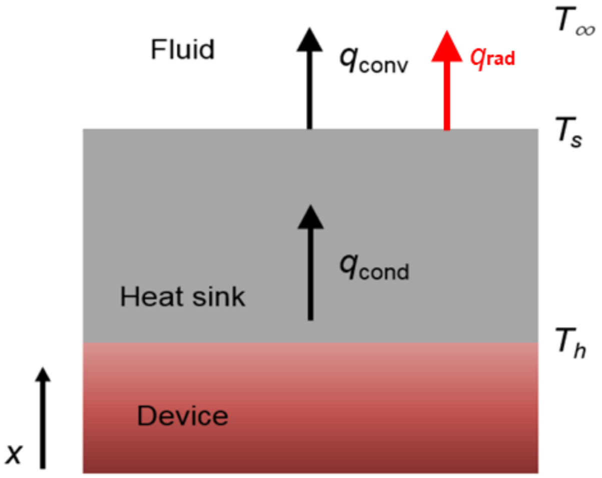

Figure 3-23. Schematic of heat transfer from heat sink to ambient air [73]

3.3.1 Co-CANP/Epoxy composite

To find out whether Co-CANP with high thermal conductivity affects heat dissipation performance, Co-CANP was used as the filler in the polymer resin used for the encapsulation of electronic devices. Epoxy novolac vinyl ester which is a polymer used for micro encapsulation of electronic devices[77] was used as matrix material, and Co-CANP which has sp^2 bonding at its skeleton frame was added. Co-CANP is expected to improve the thermal conduction inside the film, thereby increasing the rate of heat release of radiation and convection.

A thin solid film was prepared by adding bis(2,4,6-trimethylbenzoyl) phenyl phosphine oxide as photo initiator and benzoyl peroxide as thermal initiator into epoxy novolac vinyl ester resin. Amount of 0.2 wt% of photo-initiator and 1.2 wt% of thermal-initiator was added to liquid-state resin, and then stirring at room temperature on a magnetic stirring plate until additives were completely dissolved. To compare the heat dissipation performance by adding Co-CANP as a filler, Co-CANP was added at a concentration of 0.5 wt% with two kinds of initiators. After mixing, the formulation was degassed in a vacuum oven. Using UV spot light source (L9588-01, Hamamatsu photonics), thin film which has dimension of $35 \times 25 \times 11$ mm^3 was fabricated as shown in Figure 3-24. Since Co-CANP is inherently blackish material, thus the Co-CANP added film is darker than pristine film.

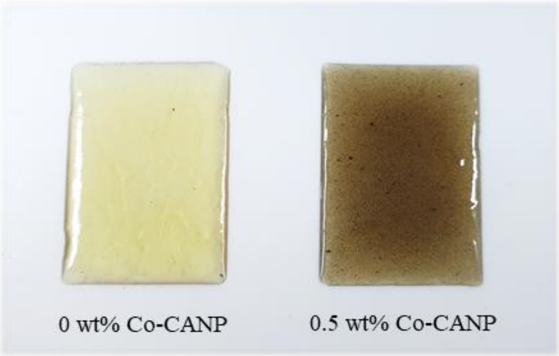

Figure 3-24. Epoxy novolac vinyl ester film with 0 wt% of Co-CANP and 0.5 wt% of Co-CANP.

3.3.2 Heat dissipation performance

The experiment consisted of placing a copper block to accelerate heat transfer to a heat sink, a plate heater that converts electrical energy into thermal energy, and placing a heat sink sample on it as shown in Figures 3-25 and 26. To reduce the resistance at the heat sink and copper block interfaces, a thin layer of silicone-based thermal grease was applied. In addition, there are three holes in the Teflon case, where a thermocouple is placed to sense temperature in real time. All the experiments were carried out in a constant temperature and humidity chamber at a temperature of 25°C and a relative humidity of 30%. By applying 12V and 0.5A of electricity to the DC power supply, the plate heater was turned on. As a result, the temperature of the upper layer of the copper block where the thermocouple is located increases. The experimental evidences for this are covered later.

To test the heat dissipation performance more accurately, five different samples were tested as shown in figure 3-27. The five experimental samples are as follows; 1. Copper block without heat sink, 2. Silicone based thermal grease applied on copper block, 3. Pristine epoxy film without thermal grease on copper block, thermal grease applied on copper block 4. with pristine epoxy film and 5. the film containing 0.5 wt% Co-CANP.

Since the surface areas of all the thin films are the same, it is expected that the heat radiation performance will be improved by radiation rather than the convection. Therefore, this will be proved through following five experiments.

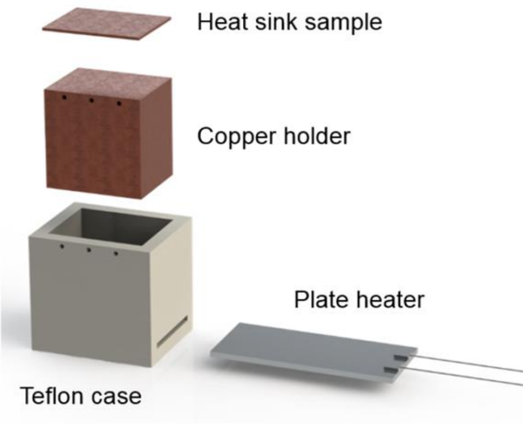

Figure 3-25. Experimental setup for heat dissipation performance test [73].

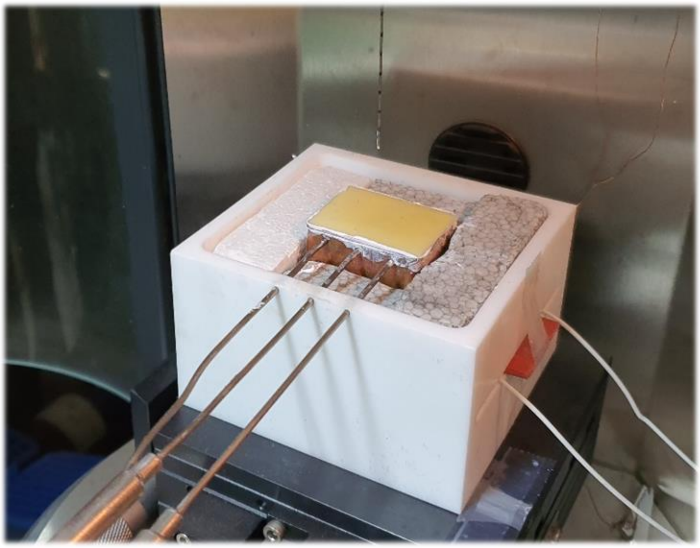

Figure 3-26. Optical image of actual experimental setup

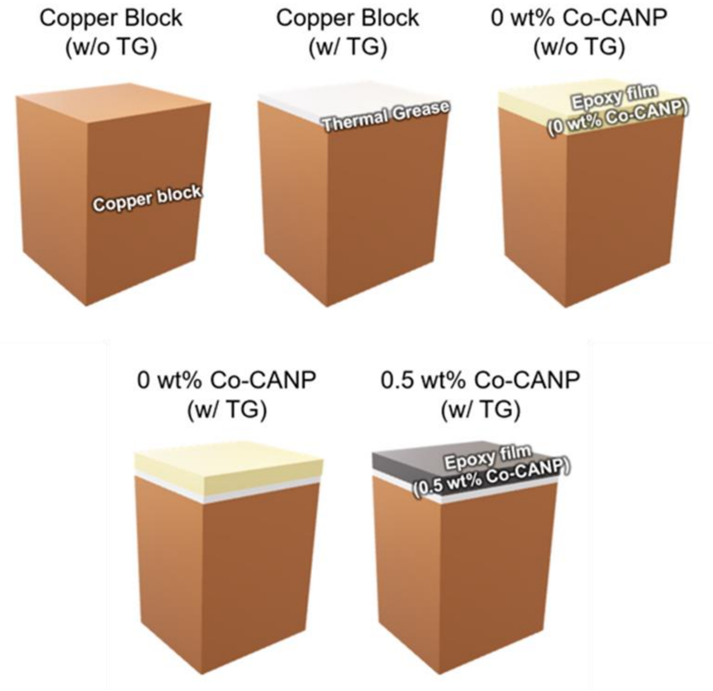

Figure 3-27. 1. Copper block without heat sink, 2. Silicone based thermal grease applied on copper block, 3. Pristine epoxy film without thermal grease on copper block, thermal grease applied on copper block 4. with pristine epoxy film and 5. the film containing 0.5 wt% Co-CANP.

After 120 minutes since turning on the plate heater, the copper block without thermal grease (w/o TG) has a surface temperature of 82.7℃ as shown in figure 3-28. In contrast, copper block with thermal grease (w/ TG) dropped to 76℃. This indicates that as the emissivity coefficient of the material constituting the surface changes, a huge difference in heat dissipation performance occurs. As shown in Table 5, copper and thermal grease, the main component of silicone rubber, differ greatly in their emissivity coefficients ($\epsilon_{copper,max} = 0.052, \epsilon_{silicone} = 0.94$). Since the emissivity coefficient has a direct influence on the amount of heat released by radiation, it can be seen that an increase in the emissivity coefficient induces an increase in the amount of heat released and thus causes more effective heat dissipation. Also, pristine epoxy film($\epsilon_{epoxy} = 0.95$) on the copper block with thermal grease (0 wt% Co-CANP (w/ TG), and pristine epoxy film without thermal grease (0 wt% Co-CANP (w/o TG)) showed a slight difference, each has surface temperature of 78℃ and 78.4 ℃ respectively. This is the result of thermal grease reducing contact resistance between the interface of the copper block and the film. Finally, the film with the 0.5 wt% Co-CANP added showed the lowest temperature of 74℃. This shows that Co-CANP uniformly distributed in the composite film contributes to the thermal conductivity improvement, and heat is released at faster rate.

Through this, it is advantageous for the heat dissipation performance to have a material such as epoxy or silicone having high thermal emissivity coefficient as a heat sink rather than a copper block. In addition, heat dissipation performance can be maximized if a material such as Co-CANP, which has high thermal conductivity, is added as a filler in a material having a high emissivity coefficient.

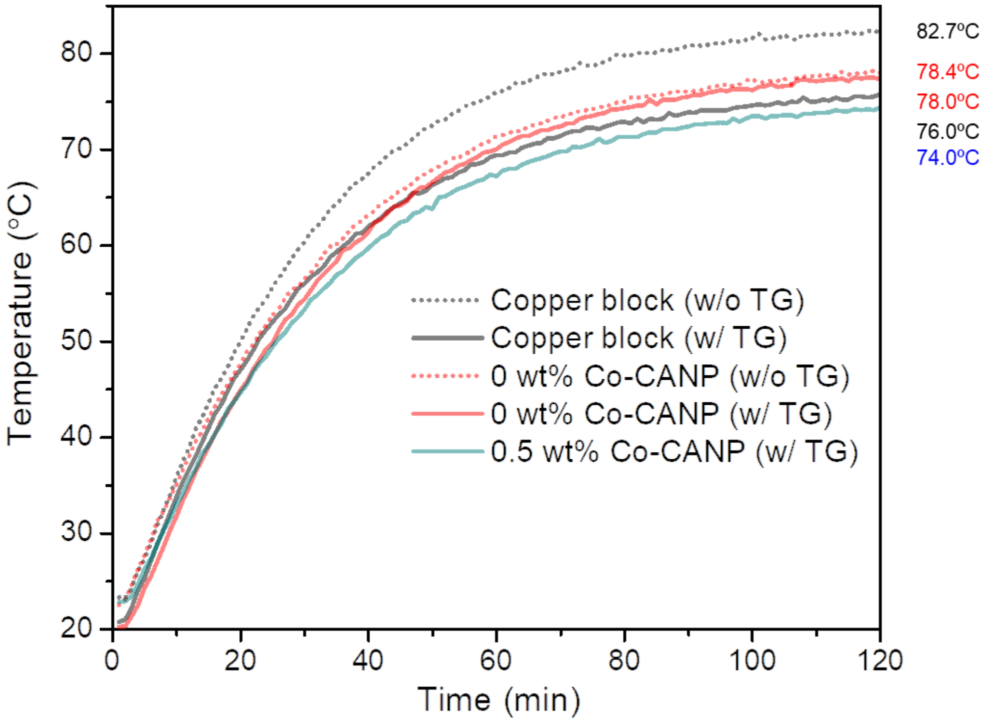

Figure 3-28. Temperature measured by thermocouples over time when electrical energy of 12 V and 0.5 A by power supply is applied to the plate heater for five test samples

Surface material	Emissivity Coefficient (ϵ)
Black body	1.00
Carbon	0.81
Copper	0.023-0.052
Silicone rubber	0.94
Epoxy	0.95

Table 5. Comparison of emissivity coefficients of the materials used in the experiment

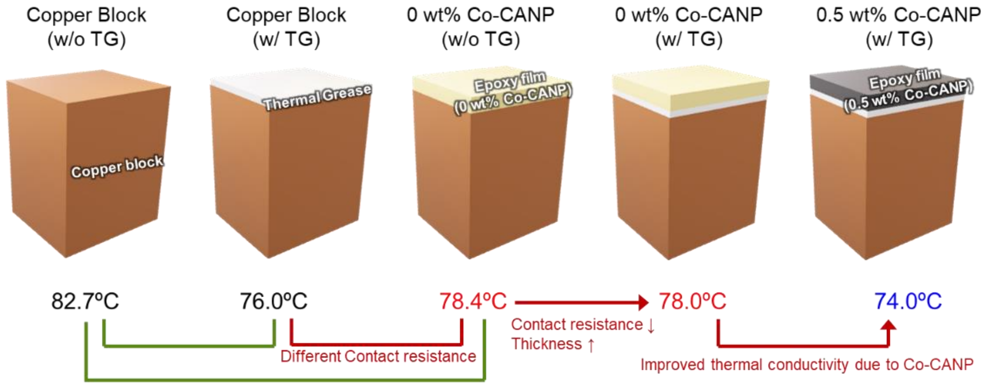

Figure 3-29. Analysis of heat dissipation test results of five different samples

Chapter 4. Conclusion

In this thesis, platform for synthesizing families of 2D materials that are co-compounded carbonaceous nanoplates (Co-CANP) is suggested. The 2D material is synthesized by a vapor-filled hydrothermal method and the reagents can be fully converted to Co-CANP, thus requiring no separation process for its use.

Co-compounding CANP with another compound can lead to rubber composites, and it is available as coating matters on the porous medium and fillers in composite materials. Functional materials were prepared by combining heterogeneous materials with Co-CANP, and the results of its performance tests were depicted in Chapter 3.

Although an organic-organic Co-CANP is considered here, organic-inorganic Co-CANPs would be a natural extension of this work, as many-compounds Co-CANPs would.

Bibliography

1. Hirsch, A., *The era of carbon allotropes.* Nature Materials, 2010. **9**(11): p. 868-871.
2. Iijima, S., *Helical Microtubules of Graphitic Carbon.* Nature, 1991. **354**(6348): p. 56-58.
3. Geim, A.K., *Graphene: Status and Prospects.* Science, 2009. **324**(5934): p. 1530-1534.
4. Dreyer, D.R., et al., *The chemistry of graphene oxide.* Chemical Society Reviews, 2010. **39**(1): p. 228-240.
5. Kratschmer, W., et al., *Solid C-60 - a New Form of Carbon.* Nature, 1990. **347**(6291): p. 354-358.
6. Baughman, R.H., A.A. Zakhidov, and W.A. de Heer, *Carbon nanotubes - the route toward applications.* Science, 2002. **297**(5582): p. 787-792.
7. De Volder, M.F.L., et al., *Carbon Nanotubes: Present and Future Commercial Applications.* Science, 2013. **339**(6119): p. 535-539.
8. Dikin, D.A., et al., *Preparation and characterization of graphene oxide paper.* Nature, 2007. **448**(7152): p. 457-460.
9. Jiao, L.Y., et al., *Narrow graphene nanoribbons from carbon nanotubes.* Nature, 2009. **458**(7240): p. 877-880.
10. Falcao, E.H.L. and F. Wudl, *Carbon allotropes: beyond graphite and*

diamond. Journal of Chemical Technology and Biotechnology, 2007. **82**(6): p. 524-531.

11. Chatterjee, C., F. Pong, and A. Sen, *Chemical conversion pathways for carbohydrates.* Green Chemistry, 2015. **17**(1): p. 40-71.

12. Kent, N.L., K.A. Rosentrater, and A.D. Evers, *Kent's technology of cereals : an introduction for students of food science and agriculture*. Fifth Edition / ed. Woodhead Publishing series in food science, technology and nutrition. 2018, Duxford: Woodhead Publishing, an imprint of Elsevier. xxiii, 900 pages.

13. Falco, C., N. Baccile, and M.M. Titirici, *Morphological and structural differences between glucose, cellulose and lignocellulosic biomass derived hydrothermal carbons.* Green Chemistry, 2011. **13**(11): p. 3273-3281.

14. Titirici, M.M., et al., *Black perspectives for a green future: hydrothermal carbons for environment protection and energy storage.* Energy & Environmental Science, 2012. **5**(5): p. 6796-6822.

15. Qian, H.S., et al., *Synthesis of uniform Te@Carbon-Rich composite nanocables with photoluminescence properties and Carbonaceous nanofibers by the hydrothermal carbonization of glucose.* Chemistry of Materials, 2006. **18**(8): p. 2102-2108.

16. Yu, S.H., et al., *From starch to metal/carbon hybrid nanostructures: Hydrothermal metal-catalyzed carbonization.* Advanced Materials,

2004. **16**(18): p. 1636-+.

17. Titirici, M.M., M. Antonietti, and N. Baccile, *Hydrothermal carbon from biomass: a comparison of the local structure from poly- to monosaccharides and pentoses/hexoses.* Green Chemistry, 2008. **10**(11): p. 1204-1212.

18. Yao, C., et al., *Hydrothermal dehydration of aqueous fructose solutions in a closed system.* Journal of Physical Chemistry C, 2007. **111**(42): p. 15141-15145.

19. Sun, X.M. and Y.D. Li, *Colloidal carbon spheres and their core/shell structures with noble-metal nanoparticles.* Angewandte Chemie-International Edition, 2004. **43**(5): p. 597-601.

20. Poerschmann, J., et al., *Hydrothermal Carbonization of Glucose, Fructose, and Xylose-Identification of Organic Products with Medium Molecular Masses.* Acs Sustainable Chemistry & Engineering, 2017. **5**(8): p. 6420-6428.

21. Kim, T., et al., *Synthesis of a Carbonaceous Two-Dimensional Material.* Acs Applied Materials & Interfaces, 2019. **11**(24): p. 21308-21313.

22. Lamer, V.K. and R.H. Dinegar, *Theory, Production and Mechanism of Formation of Monodispersed Hydrosols.* Journal of the American Chemical Society, 1950. **72**(11): p. 4847-4854.

23. Chen, L., et al., *Functional magnetic nanoparticle/clay mineral*

nanocomposites: preparation, magnetism and versatile applications. Applied Clay Science, 2016. **127**: p. 143-163.

24. Antal, M.J., W.S.L. Mok, and G.N. Richards, *Kinetic-Studies of the Reactions of Ketoses and Aldoses in Water at High-Temperature .1. Mechanism of Formation of 5-(Hydroxymethyl)-2-Furaldehyde from D-Fructose and Sucrose.* Carbohydrate Research, 1990. **199**(1): p. 91-109.
25. Baccile, N., et al., *Structural Characterization of Hydrothermal Carbon Spheres by Advanced Solid-State MAS C-13 NMR Investigations.* Journal of Physical Chemistry C, 2009. **113**(22): p. 9644-9654.
26. Balandin, A.A., *Thermal properties of graphene and nanostructured carbon materials.* Nature Materials, 2011. **10**(8): p. 569-581.
27. Pang, J.B., et al., *CVD growth of 1D and 2D sp(2) carbon nanomaterials.* Journal of Materials Science, 2016. **51**(2): p. 640-667.
28. Massiot, D., et al., *Modelling one- and two-dimensional solid-state NMR spectra.* Magnetic Resonance in Chemistry, 2002. **40**(1): p. 70-76.
29. Falco, C., et al., *Hydrothermal Carbon from Biomass: Structural Differences between Hydrothermal and Pyrolyzed Carbons via C-13 Solid State NMR.* Langmuir, 2011. **27**(23): p. 14460-14471.
30. Falco, C., et al., *Hydrothermal Carbons from Hemicellulose-Derived*

Aqueous Hydrolysis Products as Electrode Materials for Supercapacitors. Chemsuschem, 2013. **6**(2): p. 374-382.

31. Colthup, N.B., L.H. Daly, and S.E. Wiberley, *Introduction to infrared and Raman spectroscopy*. 3rd ed. 1990, Boston: Academic Press. xii, 547 p.

32. Kudin, K.N., et al., *Raman spectra of graphite oxide and functionalized graphene sheets.* Nano Letters, 2008. **8**(1): p. 36-41.

33. Yang, D., et al., *Chemical analysis of graphene oxide films after heat and chemical treatments by X-ray photoelectron and Micro-Raman spectroscopy.* Carbon, 2009. **47**(1): p. 145-152.

34. Pei, S.F. and H.M. Cheng, *The reduction of graphene oxide.* Carbon, 2012. **50**(9): p. 3210-3228.

35. Marcano, D.C., et al., *Improved Synthesis of Graphene Oxide.* Acs Nano, 2010. **4**(8): p. 4806-4814.

36. Krishnamoorthy, K., et al., *The Chemical and structural analysis of graphene oxide with different degrees of oxidation.* Carbon, 2013. **53**: p. 38-49.

37. Chen, J., et al., *An improved Hummers method for eco-friendly synthesis of graphene oxide.* Carbon, 2013. **64**: p. 225-229.

38. Mungse, H.P., et al., *Grafting of oxo-vanadium Schiff base on graphene nanosheets and its catalytic activity for the oxidation of alcohols.* Journal of Materials Chemistry, 2012. **22**(12): p. 5427-5433.

39. Yu, L.H., et al., *Carbohydrate-Derived Hydrothermal Carbons: A Thorough Characterization Study.* Langmuir, 2012. **28**(33): p. 12373-12383.

40. Ghosh, A.K. and B. Adhikari, *Reinforcing properties of a modified carbon black in NR and in an NR-NBR blend.* Kautschuk Gummi Kunststoffe, 1999. **52**(10): p. 681-688.

41. Wolff, S. and U. Gorl, *The Influence of Modified Carbon-Blacks on Viscoelastic Compound Properties.* Kautschuk Gummi Kunststoffe, 1991. **44**(10): p. 941-947.

42. Cotten, G.R., *Mixing of Carbon-Black with Rubber .1. Measurement of Dispersion Rate by Changes in Mixing Torque.* Rubber Chemistry and Technology, 1984. **57**(1): p. 118-133.

43. Choi, S.S., B.H. Park, and H. Song, *Influence of filler type and content on properties of styrene-butadiene rubber (SBR) compound reinforced with carbon black or silica.* Polymers for Advanced Technologies, 2004. **15**(3): p. 122-127.

44. Bignotti, F., et al., *Interrelation between preparation conditions, structure, and mechanical reinforcement in isoprene rubber filled with in situ generated silica.* Journal of Applied Polymer Science, 2012. **125**: p. E398-E412.

45. Mouri, H. and K. Akutagawa, *Improved tire wet traction through the use of mineral fillers.* Rubber Chemistry and Technology, 1999. **72**(5):

p. 960-968.

46. Bomal, Y., et al., *Developments in silica usage for decreased tyre rolling resistance.* Kautschuk Gummi Kunststoffe, 1997. **50**(6): p. 434-&.

47. Kong, L.H., et al., *In situ assembly of SiO2 nanodots/layered double hydroxide nanocomposite for the reinforcement of solution-polymerized butadiene styrene rubber/butadiene rubber.* Composites Science and Technology, 2018. **158**: p. 9-18.

48. Kong, L.H., et al., *High-performing multi-walled carbon nanotubes/silica nanocomposites for elastomer application.* Composites Science and Technology, 2018. **162**: p. 23-32.

49. Zhao, X.D., Y.J. Yu, and Y.J. Wu, *Improving low-frequency sound absorption of micro-perforated panel absorbers by using mechanical impedance plate combined with Helmholtz resonators.* Applied Acoustics, 2016. **114**: p. 92-98.

50. Zhai, W., et al., *Microstructure-based experimental and numerical investigations on the sound absorption property of open-cell metallic foams manufactured by a template replication technique.* Materials & Design, 2018. **137**: p. 108-116.

51. Cao, L.T., et al., *Porous materials for sound absorption.* Composites Communications, 2018. **10**: p. 25-35.

52. Bujoreanu, C., et al., *Experimental and theoretical considerations on*

sound absorption performance of waste materials including the effect of backing plates. Applied Acoustics, 2017. **119**: p. 88-93.

53. Nine, M.J., et al., *Graphene Oxide-Based Lamella Network for Enhanced Sound Absorption.* Advanced Functional Materials, 2017. **27**(46).

54. Rahimabady, M., et al., *Hybrid local piezoelectric and conductive functions for high performance airborne sound absorption.* Applied Physics Letters, 2017. **111**(24).

55. Lu, B., et al., *High performance broadband acoustic absorption and sound sensing of a bubbled graphene monolith.* Journal of Materials Chemistry A, 2019. **7**(18): p. 11423-11429.

56. Lu, T.J., F. Chen, and D.P. He, *Sound absorption of cellular metals with semiopen cells.* Journal of the Acoustical Society of America, 2000. **108**(4): p. 1697-1709.

57. Vorländer, M., *Auralization : fundamentals of acoustics, modelling, simulation, algorithms and acoustic virtual reality*. 1st ed. 2008, Berlin: Springer. x, 335 p.

58. Fouladi, M.H., M. Ayub, and M.J.M. Nor, *Analysis of coir fiber acoustical characteristics.* Applied Acoustics, 2011. **72**(1): p. 35-42.

59. Prasher, R., *Thermal interface materials: Historical perspective, status, and future directions.* Proceedings of the Ieee, 2006. **94**(8): p. 1571-1586.

60. Renteria, J.D., D.L. Nika, and A.A. Balandin, *Graphene Thermal Properties: Applications in Thermal Management and Energy Storage.* Applied Sciences-Basel, 2014. **4**(4): p. 525-547.

61. Lin, W.T., et al., *The thermal evaluation of the substrate mixed with microencapsulated phase change materials for MEMS packaging applications.* Microsystem Technologies-Micro-and Nanosystems-Information Storage and Processing Systems, 2011. **17**(4): p. 693-699.

62. Arik, M. and A. Setlur, *Environmental and economical impact of LED lighting systems and effect of thermal management.* International Journal of Energy Research, 2010. **34**(13): p. 1195-1204.

63. Zhang, P., et al., *Thermal Properties of Graphene Filled Polymer Composite Thermal Interface Materials.* Macromolecular Materials and Engineering, 2017. **302**(9).

64. Lee, J.S., et al., *Efficient heat dissipation by ion-mediation assembled reduced graphene oxide.* Journal of Materials Chemistry C, 2018. **6**(10): p. 2515-2521.

65. Zhang, G., et al., *Excellent heat dissipation properties of the super-aligned carbon nanotube films.* Rsc Advances, 2016. **6**(66): p. 61686-61694.

66. Yu, W., et al., *Effect of an Auxiliary Plate on Passive Heat Dissipation of Carbon Nanotube-Based Materials.* Nano Letters, 2018. **18**(3): p. 1770-1776.

67. Zou, Y.C., et al., *Al2O3/reduced graphene oxide double-layer radiative coating for efficient heat dissipation.* Materials & Design, 2018. **157**: p. 130-140.

68. Zou, Y.C., et al., *Facile One-Step Fabrication of Multilayer Nanocomposite Coating for Radiative Heat Dissipation.* Acs Applied Electronic Materials, 2019. **1**(8): p. 1527-1537.

69. Kordas, K., et al., *Chip cooling with integrated carbon nanotube microfin architectures.* Applied Physics Letters, 2007. **90**(12).

70. Lin, Y.F., C.T. Hsieh, and R.J. Wai, *Facile synthesis of graphene sheets for heat sink application.* Solid State Sciences, 2015. **43**: p. 22-27.

71. Huang, Z.L., et al., *Microstructure dependence of heat sink constructed by carbon nanotubes for chip cooling.* Journal of Applied Physics, 2015. **117**(2).

72. Lienhard, J.H. and J.H. Lienhard, *A heat transfer textbook*. Corrected, revised, and updated fifth edition. ed. 2019, Mineola: Dover Publications, Inc. pages cm.

73. Kim, T., *Metal-graphene Oxide Coordination Network.* 서울대학교 대학원, 2016. **Doctoral dissertation**.

74. Toolbox, E., *Emissivity Coefficients Materials.* 2003.

75. Brewster, M.Q., *Thermal radiative transfer and properties*. 1992,

New York: Wiley. xxii, 543 p.

76. Webster, J.G., *The measurement, instrumentation, and sensors handbook*. The electrical engineering handbook series. 1999, Boca Raton, Fla.: CRC Press published in cooperation with IEEE Press.

77. Baikerikar, K.K. and A.B. Scranton, *Photopolymerizable liquid encapsulants for microelectronic devices: Thermal and mechanical properties of systems with reduced in-mold cure times.* Journal of Applied Polymer Science, 2001. **81**(14): p. 3449-3461.

초 록

2차원 혼성 복합체 나노플레이트

송혜린
기계항공공학부
서울대학교

탄소 동소체 중 하나인 그래핀의 발견은 2차원 재료에 대한 막대한 관심을 불러일으켰다. 2차원 재료는 높은 종횡비를 갖는 비표면적이 매우 큰 물질로써, 그 응용성이 무궁무진하다. 다양한 원소를 기반으로 한 2차원 재료들이 보고되고 있지만, 거의 대부분 시작물질의 특성을 벗어나지 못한 채 top-down 방식으로 2차원 재료를 얻고 있는 실정이다.

이 논문에서는 두가지 이상의 화합물을 반응 물질로 사용하여, 물질 특성이 조절 가능한 2차원 재료를 합성하는 방식에 대해 소개하고자 한다. 이는 Bottom-up 방식의 새로운 2차원 물질 합성 플랫폼이며, 반응에 참가하는 화합물의 종류에 따라 합성되어지는 혼성복합질 나노플레이트의 특성이 조절된다는 큰 장점이 있다. 기능기를 갖는 화합물은 모두 반응물질의 후보가 될 수 있으며, 포도당만을 사용하여 2차원 물질을 합성했을 때보다 더 많은 수의

sp^2 결합을 갖는 2차원 물질을 합성하였다. 본 논문에서는 포도당(glucose)을 핵 생성(nucleation) 물질로 사용하고 카테콜(dihydroxy benzene)을 추가적인 반응 물질로 사용하여 혼성복합질 탄소질 나노플레이트를 합성하였다. 다양한 분석 기법을 통해 물질 특성을 확인하였으며, 이를 여러 응용성 재료에 첨가물질로 사용하여 그 효능을 검증하였다.

주요어: 혼성복합질 재료 · 2차원 재료·나노플레이트 · 탄소질 재료 · 수열탄화 · 물질 합성 플랫폼

학 번: 2014-30364